Molecular Therapy
Original Article

Waning efficacy in a long-term AAV-mediated gene therapy study in the murine model of Krabbe disease

Gregory J. Heller,[1,7] Michael S. Marshall,[1,7] Yazan Issa,[1] Jeffrey N. Marshall,[1] Duc Nguyen,[1] Emily Rue,[2] Koralege C. Pathmasiri,[3] Miriam S. Domowicz,[4] Richard B. van Breemen,[2] Leon M. Tai,[1] Stephanie M. Cologna,[3] Stephen J. Crocker,[5] Maria I. Givogri,[1] Mark S. Sands,[6] and Ernesto R. Bongarzone[1]

[1]Department of Anatomy and Cell Biology, College of Medicine, University of Illinois at Chicago, Chicago, IL 60612, USA; [2]Linus Pauling Institute, Oregon State University, Corvallis, OR 97331, USA; [3]Department of Chemistry, University of Illinois at Chicago, Chicago, IL 60607, USA; [4]Department of Pediatrics, University of Chicago, Chicago, IL 60612, USA; [5]Department of Neuroscience, University of Connecticut School of Medicine, Farmington, CT 06030, USA; [6]Department of Medicine, Washington University in St. Louis, St. Louis, MO 63110, USA

Neonatal AAV9-gene therapy of the lysosomal enzyme galactosylceramidase (GALC) significantly ameliorates central and peripheral neuropathology, prolongs survival, and largely normalizes motor deficits in Twitcher mice. Despite these therapeutic milestones, new observations identified the presence of multiple small focal demyelinating areas in the brain after 6–8 months. These lesions are in stark contrast to the diffuse, global demyelination that affects the brain of naive Twitcher mice. Late-onset lesions exhibited lysosomal alterations with reduced expression of GALC and increased psychosine levels. Furthermore, we found that lesions were closely associated with the extravasation of plasma fibrinogen and activation of the fibrinogen-BMP-SMAD-GFAP gliotic response. Extravasation of fibrinogen correlated with tight junction disruptions of the vasculature within the lesioned areas. The lesions were surrounded by normal appearing white matter. Our study shows that the dysregulation of therapeutic GALC was likely driven by the exhaustion of therapeutic AAV episomal DNA within the lesions, paralleling the presence of proliferating oligodendrocyte progenitors and glia. We believe that this is the first demonstration of diminishing expression *in vivo* from an AAV gene therapy vector with detrimental effects in the brain of a lysosomal storage disease animal model. The development of this phenotype linking localized loss of GALC activity with relapsing neuropathology in the adult brain of neonatally AAV-gene therapy-treated Twitcher mice identifies and alerts to possible late-onset reductions of AAV efficacy, with implications to other genetic leukodystrophies.

INTRODUCTION

Globoid cell leukodystrophy, or Krabbe disease (KD), is a lysosomal storage disorder caused by the loss of function of the lysosomal enzyme galactosylceramidase (GALC),[1] resulting in the abnormal accumulation of the GALC substrate psychosine.[2–4] Most affected patients are newborns developing diffuse central and peripheral sclerosis (demyelination),[5] with neurosensory deficits and muscle atrophy, leading to death within the first few years of life.[6]

Recent efforts have focused on the development of gene therapy protocols that aim to replace the deficient GALC enzyme. Previous studies have been successful in delaying the onset of demyelination, motor deficits, and significantly prolonging survival.[7–14] A study published by our group used a high-dose gene therapy regimen with codon-optimized murine *Galc* packaged in an adeno-associated virus, serotype 9 capsid (AAV9-GALC) and globally delivered via intracranial (i.c.), intrathecal (i.t.), and intravenous (i.v.) injections in the Twitcher (TWI) mouse model of KD. Treated TWI mice showed few to no signs of disease for most of their lifespan, which was significantly lengthened from a 44-day median survival to 265 days, with maximal survival of 650 days.[7]

We investigated the factors influencing the long-term survival of AAV9-GALC treated TWI and we determined that there is a late-onset manifestation of the sclerotic phenotype, which is limited to small and well-defined portions in the brain. Instead of the diffuse demyelination traditionally observed in the brain of untreated TWI, multiple focal lesions of demyelination engulfed by gliotic scarring were found in brain white matter. These lesions exhibited a localized neuroinflammatory state featuring the proliferation of

Received 4 November 2020; accepted 21 January 2021;
https://doi.org/10.1016/j.ymthe.2021.01.026.

[7]These authors contributed equally

Correspondence: Michael S. Marshall, PhD, Department of Pathology, Massachusetts General Hospital, 55 Fruit St., Boston, MA 02114, USA.
E-mail: mmarshall@mgh.harvard.edu
Correspondence: Ernesto R. Bongarzone, Department of Anatomy and Cell Biology, College of Medicine, University of Illinois at Chicago, 808 S. Wood St., M/C 512, Chicago, IL 60612, USA.
E-mail: ebongarz@uic.edu

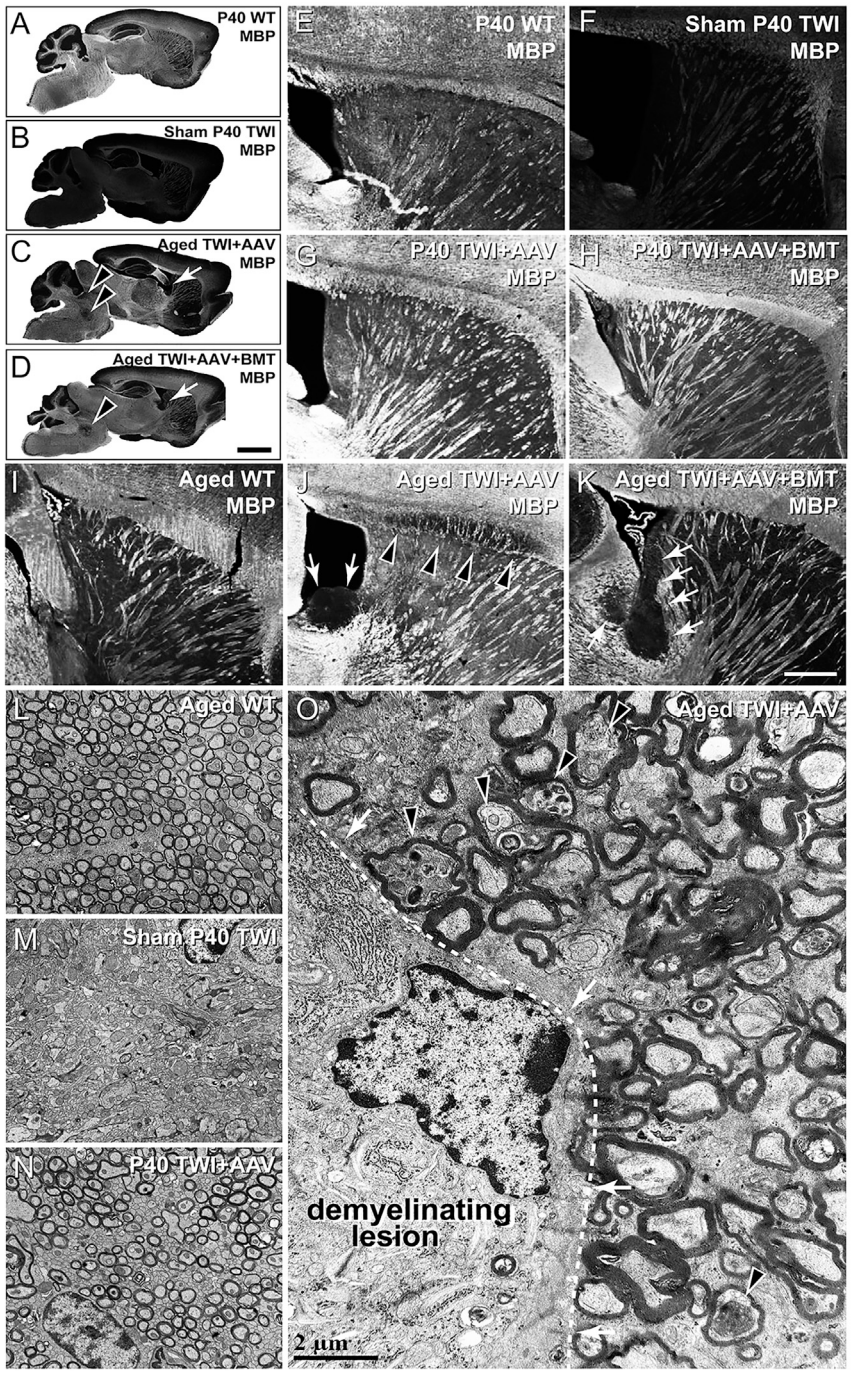

Figure 1. Multi-focal lesions in the brain of aged TWI treated with AAV9-GALC

(A–D) MBP-stained sagittal whole-brain scans of P40 WT (A), sham P40 TWI (B), aged TWI+AAV (C), and aged TWI+AAV+BMT (D). In both TWI+AAV (C) and TWI+AAV+BMT (D), multi-focal demyelinating lesions were observed. Tissue adjacent to the lateral ventricle (arrows) was affected in all aged animals examined; brainstem (arrowheads), corpus callosum, and cerebellum were also commonly affected. (E–H) Higher-magnification images of MBP-stained P40 WT (E), sham P40 TWI (F), P40 TWI+AAV (G), and P40 TWI+AAV+BMT (H). At this age, neither TWI+AAV nor TWI+AAV+BMT animals display any demyelinating lesions. (I–K) Higher-magnification images of MBP-stained aged WT (I), aged TWI+AAV (J), and aged TWI+AAV+BMT (K). The demyelinating lesions are evident in the stria terminals near the lateral ventricle (arrows) and corpus callosum (arrowheads). (L–O) Electron microscopy imaging was used to examine myelin structure between aged WT (L), sham P40 TWI (M), P40 TWI+AAV (N), and an aged TWI+AAV (O). No evidence of demyelination was detected in P40 TWI+AAV at P40 (N), displaying similar structure to a WT animal (L). Areas of demyelination in aged TWI+AAV (O) were similar in appearance to the diffuse demyelination seen in sham TWI (M); however, the damage was localized and displayed sharp demarcations between affected and unaffected tissue (O, dashed line, arrows). Evidence of axonal stress was also detected (arrowheads). Scale bars, (A)–(D) 1.5 mm; (E)–(K) 100 μm; (L)–(O) 2 μm.

oligodendrocyte progenitor cells (OPCs), astrocytes, and microglia. Expression of the GALC transgene declined in the lesions and was accompanied by increased levels of psychosine. Analysis of treated TWI animals at a younger age (i.e., 40 days of age) did not reveal any evidence of focal demyelinating lesions, indicating that this phenotype arises as a late-onset phenomenon.

The observations presented in this study hold important implications for understanding the possible long-term safety of AAV gene therapy for KD and emphasize the need for continuous monitoring and improvement of therapeutic protocols and strategies for KD and other genetic leukodystrophies.

RESULTS

Late-onset multifocal demyelination in the brain of AAV9-GALC-treated TWI mice

TWI (GALC-deficient) mice were treated with a global AAV9-GALC gene therapy regimen (i.c., i.v., and i.t.) after birth, as previously described.[7] The AAV9-GALC therapy was compared alongside an analog (bone marrow transplantation, BMT)[9,11,14,15] of the current best clinical practice (hematopoietic stem cell transplantation, HSCT),[16–18] both alone and in combination with one another.

The TWI mouse displays diffuse demyelination throughout the CNS (Figures 1B and 1F) and peripheral nervous system (PNS) (Figures S1A and S1B), confirmed histologically in sham-treated TWI mice (sham TWI). AAV9-GALC gene therapy, globally administered in a high-dose regimen forestalled this demyelination at P40 both alone (TWI+AAV) (Figure 1G) or in combination with BMT

(TWI+AAV+BMT) (Figure 1H) to levels indistinguishable from a wild-type (WT) P40 animal (Figure 1E). The PNS was equally protected at the P40 time point (Figures S1E and S1F) by AAV9-GALC to levels compatible with WT (Figures S1C and S1D).

As reported by Marshall et al.,[7] brain tissue from aged (180 days or older) TWI+AAV (Figure 1C) and TWI+AAV+BMT (Figure 1D) showed a global well-preserved myelination comparable to WT brains (Figure 1A), underscoring the power of GALC correction following neonatal gene therapy. A closer inspection of aged, treated TWI brains revealed the presence of multiple (ranging 2–8 lesions per brain), distinct regions of focal demyelination (0.5–2 mm^3) (Figures 1C and 1D, arrows and arrowheads). Within the lesions, there was a complete loss of myelin, confirmed by both myelin basic protein (MBP) staining (Figures 1J and 1K, arrows and arrowheads) and by electron microscopy (EM) (Figure 1O). EM identified the ultrastructure of these lesions, highlighting the stark delineation between healthy and demyelinated tissue (Figure 1O, dotted line and arrows). Within the demyelinated lesions, damaged tissue in aged TWI+AAV animals (Figure 1O) had a similar structure to the diffuse damage seen in sham P40 TWI (Figure 1M). Axons with thin myelin layers, suggestive of a remyelination process,[19] were not found in the lesions, indicating that these lesions progressively worsened without evidence of remission or effective myelin repair. Areas adjacent to the lesions (Figures 1C, 1D, 1J, 1K, and 1O) remained relatively intact and normal appearing, comparable to aged WT (Figures 1A, 1I, and 1L) and the P40 TWI+AAV (Figures 1G, 1H, and 1N); however, there was some evidence of axonal stress (e.g., axonal swelling) in axons adjacent to lesions (Figure 1O, arrowheads).

Not all regions of the brain were affected equally. Myelinated tracts of the stria terminalis (Figures 1C, 1D, 1J, and 1K, arrows) were affected in all animals. Other affected regions included cerebellar and brainstem white matter (Figures 1C and 1D, arrowheads) and corpus callosum (Figure 1J, arrowheads). Lesions were identified in the brains of all AAV9-GALC-treated animals examined (6 total examined: 3 TWI+AAV, 3 TWI+AAV+BMT). Plaques were not present in any of the brains of treated TWI evaluated at earlier ages (P40; n = 5). Within the CNS, this localized demyelination was present only in the brain. Serial sections from spinal cords from both TWI+AAV and TWI+AAV+BMT animals were examined and showed no evidence of focal demyelination (Figure S2). In addition, focal demyelination was not observed within the PNS of aged TWI+AAV (Figures S1G and S1H) or TWI+AAV+BMT animals (data not shown).

In our previous paper,[7] we showed that AAV alone or in combination with BMT ameliorated signs of disease for the first 6–8 months of life through our clinical disease scoring system. The clinical disease score is composed of three components: mass change (which was shown in our previous report[7]), presence of tremor, and locomotor ability. To better understand when pathology and signs of disease begin, locomotor ability and tremor in relation to age were quantified over time (Figures S3A and S3B). This showed that tremor begins in most TWI+AAV and TWI+AAV+BMT animals at ~16 weeks of age and locomotor ability begins to decline at ~20 weeks of age. This suggests that although these animals display an overall pronounced and lasting clinical improvement and increased survival, there are clinical deteriorations that can be appreciated during these animals' aging.

Multiple studies have used an AAV gene therapy to treat TWI mice, but only two reports[11,14] have presented some imaged evidence of analogous myelin lesions in the CNS of AAV-treated TWI mice. It is important to note the differences in gene therapy design, methodology, and time of analysis between these two studies and ours. Hawkins-Salsbury et al.[14] used a combination of L-cycloserine, BMT, and AAV2/5-GALC. Mice received gene therapy (i.c., 6×10^9 vector genomes [vg]/mouse and i.t., 1.5×10^{10} vg/mouse) between post-natal days (P)2 and 3, followed by BMT on P4 and L-cycloserine (an irreversible inhibitor 3-ketodehydrosphingosine synthase, ultimately leading to decreased psychosine[20]) treatment starting at P5–7 for the life of the animal. Histological analyses of myelin were done on P160. In contrast, Karumuthil-Melethil et al.[11] compared AAV9, AAV001, and AAVrh10 administered i.t. (2×10^{11} vg/mouse) on P11, with histological analyses performed at P35. Despite these methodological differences, both studies presented some evidence of focal lesions after an initial healthy period in treated TWI, but further analysis was not reported. To provide unbiased cross-examination of our study, we examined an independent set of TWI mice produced by the Sands lab and subjected to a triple combined treatment analogous to that reported previously by that lab,[14] with the relevant difference that AAV2/5-GALC was replaced with the same AAV9-GALC vector used in this present study (Figure S4). At P35, myelination in treated TWI (Figure S4C) appeared indistinguishable from WT (Figure S4A) compared to untreated TWI (Figure S4B). However, multifocal demyelinated lesions were evident in the brain of aged, treated TWI. Example images of demyelinating lesions in the corpus callosum are shown at P160 (Figure S4D, arrows) and terminal P500 (Figures S4E and S4F, arrows). These findings from an independent study indicate that these multi-focal lesions are not protocol dependent and are a potential comorbidity of AAV gene therapy in different contexts.

Reduced expression of therapeutic GALC enzyme and accumulation of psychosine in focal demyelinated lesions

To understand the cause(s) of these lesions, we aimed to determine whether the expression of therapeutic GALC was compromised in lesioned areas. Fluorescent *in situ* hybridization (FISH) using a riboprobe specifically designed to recognize the mouse *Galc* mRNA confirmed the robust expression of therapeutic *Galc* mRNA throughout the brain of P40 TWI+AAV+BMT (Figures 2B and 2G), but a total absence of *Galc* mRNA in the sham TWI brain (Figures 2A and 2F). Expression in P40-treated TWI is close to that observed in WT brains (Figures 2D and 2I). In contrast, ISH in lesioned areas (e.g., corpus callosum, brainstem) of aged AAV-treated TWI brains revealed regions with significant reductions of *Galc* mRNA expression (Figures 2C and 2H, dotted lines). Specificity and background binding levels of the probes are displayed as well (Figures 2E and 2J).

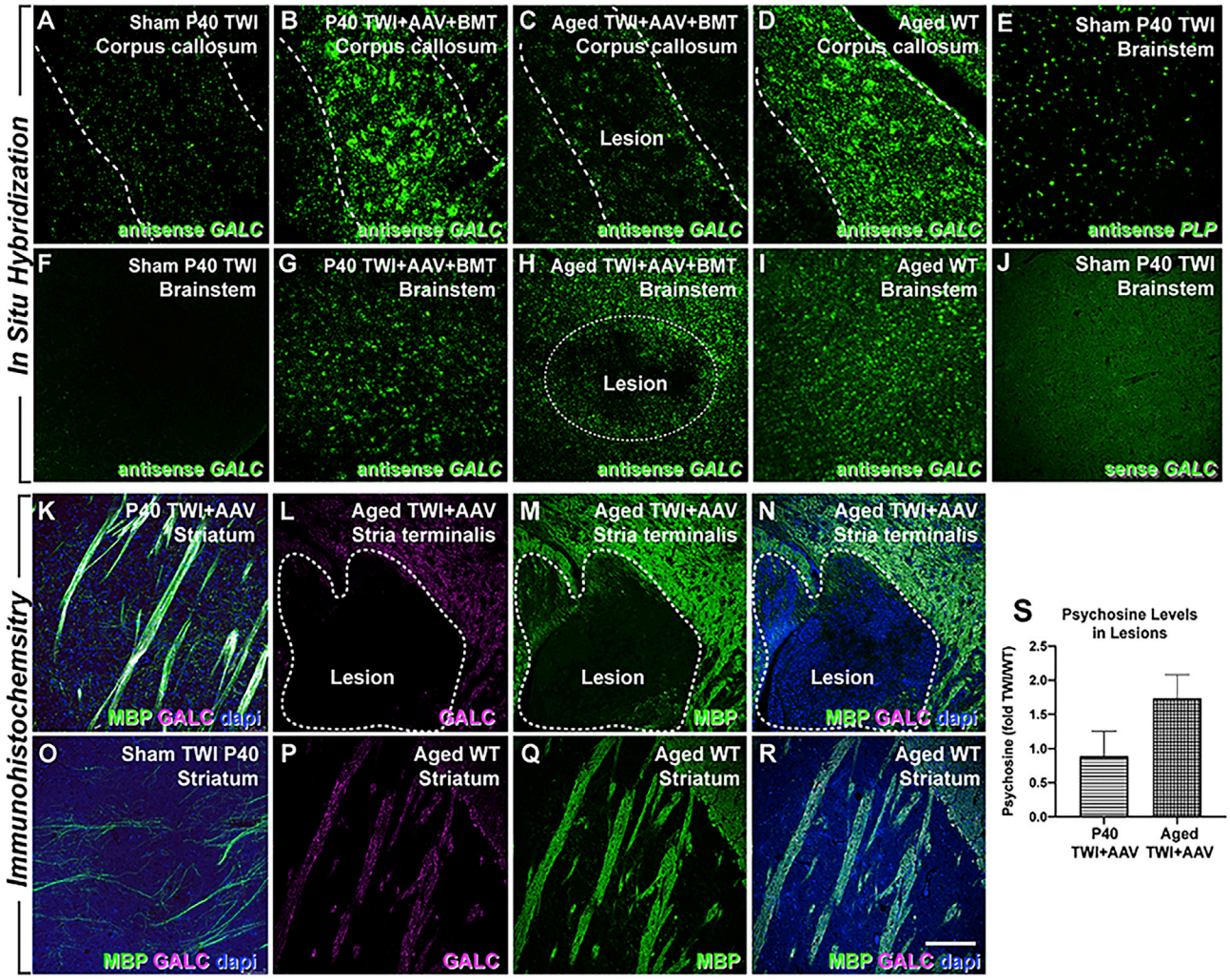

Figure 2. Focal loss of GALC expression within demyelinating lesions

(A, B, D, F, G, and I) *In situ* hybridization using antisense probes recognizing GALC demonstrates the lack of expression of *GALC* mRNA within the brains of the sham P40 TWI (A and F), while P40 TWI+AAV+BMT (B and G) and aged WT (D and I) mice showed robust *GALC* expression in 2 regions that were common for lesions to occur: the corpus callosum and the brainstem. (C, E, H, and J) Aged TWI+AAV animals were found to have a significant reduction in *GALC* expression in lesion sites in these 2 regions (C and H, dotted line). Background binding levels of sense probes (J) and its specificity (E) are displayed as well. (K–R) Immunohistochemical staining for MBP (green) and GALC (purple) showed show limited MBP and GALC staining in sham TWI brain (O) in comparison to P40 TWI+AAV (K) and WT (P–R) mice. Minimal GALC (L) and MBP staining (M) was detected within lesions in aged TWI+AAV mice (L–N, dotted line). (S) Psychosine levels measured from micropunches within the lesion areas from P40 and aged TWI+AAV and normalized to levels in WT (n = 3 per group). Scale bars: 100 μm.

The localized decline of *Galc* mRNA was accompanied by analogous decreases in the levels of GALC protein immunodetected within lesions of aged, treated TWI brains. This staining shows the absence of GALC immunoreaction within a lesion of an aged TWI+AAV (Figure 2L, inside dotted lines). The lesion was identified by its lack of immunoreaction to anti-MBP antibodies (Figure 2M). The lesions were noted to be hypercellular via DAPI staining (Figure 2N). GALC protein was immunodetected in non-lesioned areas of aged, treated TWI brains (Figure 2L, outside dotted lines), P40-treated TWI brains (Figure 2K), and aged WT brains (Figures 2P–2R), but not in sham TWI (Figure 2O). These results provide evidence that demyelinating lesions are associated with areas in the TWI brain where GALC expression was initially restored by AAV9-GALC therapy, but subsequently declined during aging.

To have a measure of the functional effect of this localized decline of expression of therapeutic GALC, serial sections of treated TWI brains were subjected to micropunches and liquid chromatography-tandem mass spectrometry (LC-MS/MS) for the detection of psychosine levels. Figure 2S shows that, albeit not reaching statistical significance, lesioned areas of the aged TWI+AAV brain contained detectable levels of psychosine that were elevated as compared to younger P40 TWI+AAV.

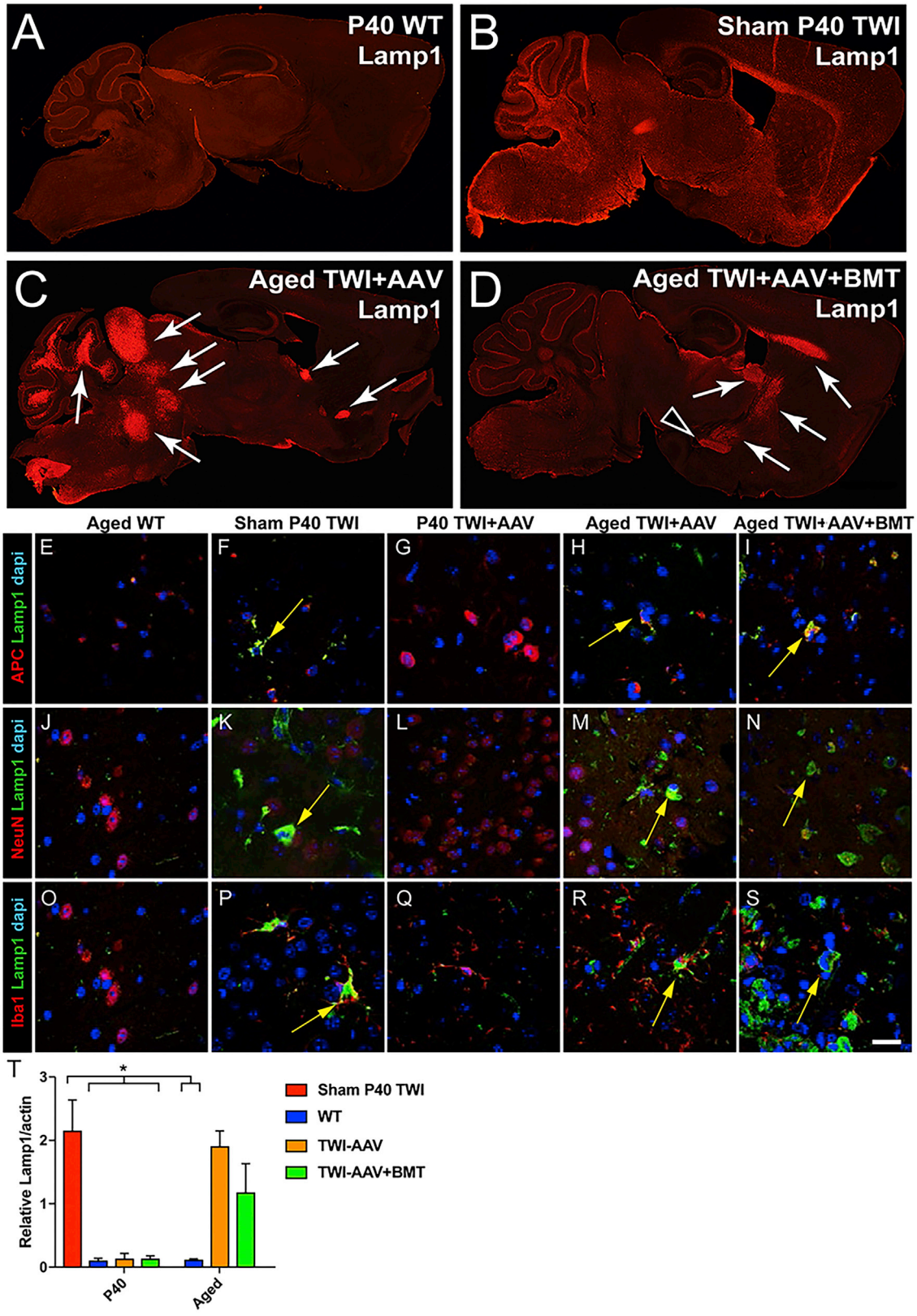

(legend on next page)

These analyses provide evidence that localized deficits of GALC activity developed in defined regions of the treated adult TWI brain.

Reduction of GALC expression associated with relapse of lysosomal responses in focal demyelinated lesions

In naive TWI brains, the lack of GALC expression is always accompanied by abnormal lysosomal responses,[7] including exacerbated expression of lysosomal proteins such as LAMP1 and the presence of abundant lysosomal structures throughout the brain (Figure 3B). Aberrant lysosomal responses were detected in multiple brain cell types, including oligodendrocytes (Figures 3E–3I), neurons (Figures 3J–3N), and microglia (Figures 3O–3S). WT brains (Figures 3A, 3E, 3J, and 3O) do not display these abnormal lysosomal responses. Immunofluorescent staining for LAMP1 revealed a multifaceted pathology within the focal demyelinated areas of the aged AAV9-GALC-treated TWI (Figures 3C and 3D). Compared with WT (Figures 3A, 3E, 3J, and 3O) and sham TWI (Figures 3B, 3E, 3J, and 3O), gene therapy successfully corrected lysosomal responses in oligodendrocytes, neurons, and microglia throughout the brain of TWI+AAV animals at P40 (Figures 3G, 3L, and 3Q). In stark contrast, brain tissue from aged TWI+AAV and TWI+AAV+BMT had abundant LAMP1$^+$ material accumulated, indicating a return to a pathological state in oligodendrocytes (Figures 3H and 3I), neurons (Figures 3M and 3N), and microglia (Figures 3R and 3S). Quantification (Figure 3T) of LAMP1 expression confirmed that the robust correction of LAMP1 observed at P40 weakened in aged, treated TWI. These results indicate the resurgence of lysosomal dysfunction in focal brain areas during the aging of treated TWI.

Adult-onset lesions are robustly microgliotic and exhibit fibrinogen extravasation

Remyelination is known to occur within TWI, as normal repair mechanisms attempt to replace damaged myelin.[21] This includes the recruitment of inflammatory cells such as microglia,[21] which was observed to occur in these lesions, creating glial scarring around the lesion margins (Figure 4C, arrows) in comparison to WT (Figure 4B) and sham TWI (Figure 4A) brains. Localized damage to white matter is usually associated with leakage of the blood-brain barrier (BBB).[22–26] In fact, extravasation of plasma proteins, particularly fibrinogen into the brain, has been reported to act as a mediator of microglial activation and damage in multiple neurological conditions,[27,28] including disorders with multi-focal demyelination such as multiple sclerosis.[29] Plasma protein leakage was initially assessed with an antibody-recognizing fibrinogen, revealing extensive fibrinogen involvement within lesions of aged TWI+AAV (Figure 4F, arrow). Sites of fibrinogen extravasation were populated by activated IBA1$^+$ microglia and highly restricted to demyelinated lesion areas (Figures 4G–4I, arrow). Fibrinogen leakage was not observed in sham TWI or WT aged animals (Figures 4D and 4E). Leakage of plasma proteins was not observed in the spinal cord (Figure S5), which was consistent with an absence of lesions (Figure S2).

Activation of the fibrinogen-SMAD pathway facilitates a potent inflammatory glial response in adult-onset lesions

Extravasation of fibrinogen is a common finding in the lesioned brain regions of patients with multiple sclerosis and ischemic injury, and this extravasated fibrinogen is associated with astrogliosis.[22–27,30] Recent findings have shown that extravasated fibrinogen promotes shifting neural progenitors' fate to astrocytes by activation of the bone morphogenic protein (BMP) pathway.[31] We assessed the involvement of these responses in the neuropathology observed in the brain of aged, treated TWI mice. We used immunohistochemistry to examine the association between fibrinogen in demyelinating lesions with glial fibrillary acidic protein (GFAP). We detected a strong gliotic response with abundant GFAP$^+$ astrocytes (Figure 5A) engulfing lesioned areas containing immunodetectable fibrinogen (Figures 5B and 5C). This gliotic response was in stark contrast to areas devoid of demyelinated lesions in the aged brains of TWI+AAV, which lacked any detectable fibrinogen and GFAP astrogliosis, such as the striatum (Figures 5D–5F), and to the generalized gliosis observed throughout the brains of the sham TWI (Figures 5G–5I). We did not find significant differences in astrocyte responses between P40 TWI+AAV (Figure 5J) and adult WT (Figure 5K), strongly suggesting that astrogliosis and fibrinogen extravasation in lesions developed together during aging of the treated TWI. Secondary antibody controls are shown in Figure 5L. Quantification of these responses showed significant increases in GFAP in aged TWI+AAV brains (Figure 5X) and of the alpha unit of fibrinogen (Figure 5V). Inflammatory astrogliosis in aged, treated TWI was further confirmed by the quantification of the levels of Serpina3 and LCN2, two known proteins involved in the activation of astrogliosis in multiple sclerosis,[32,33] revealing significant upregulations (Figures 5Y and 5Z) in the aged, treated TWI brains. These results confirm the activation of a strong inflammatory response in these mice.

Immunohistochemistry for SMAD1 showed strong reactivity within the demyelinated lesions of the aged AAV-treated TWI brain (Figures 5M–5O). As expected, SMAD1 reactivity was strongly associated with gliotic GFAP$^+$ detection (Figures 5P–5R) and fibrinogen (Figures 5S–5U). Phosphorylation of SMAD1 at Ser 463/465 is a readout of the

Figure 3. Lysosomal abnormalities relapse in aged, treated TWI

Staining for the lysosomal marker LAMP1 was used as a readout of lysosomal stress. (A–D) LAMP1 staining of sagittal brain slices depicts robust lysosomal accumulations (arrows) associated with the lesions of aged TWI+AAV (C) and TWI+AAV+BMT (D) in contrast to widespread lysosomal accumulation within sham P40 TWI (B) and control levels in P40 WT (A). (E–S) Tissue was double-stained for LAMP1 as well as cell-specific markers APC (E–I, oligodendrocytes), NeuN (J–N, neurons), and IBA1 (O–S, microglia). LAMP1 accumulation (arrows) was observed in oligodendrocytes, neurons, and microglia of sham P40 TWI (F, K, and P), while it was minimal in WT tissue (E, J, and O). Lysosomal accumulations were not evident in P40 TWI+AAV (G, L, and Q) but were seen in oligodendrocytes, neurons, and microglia located within the lesions of aged TWI+AAV (H, M, and R) or TWI+AAV+BMT (I, N, and S). In addition, quantitative western blots of LAMP1 expression (T) confirmed increased LAMP1 levels in aged, treated TWI brains (n = 4–6; *$p < 0.05$). Scale bars: (A–D) 1.5 mm; (E–S) 30 μm.

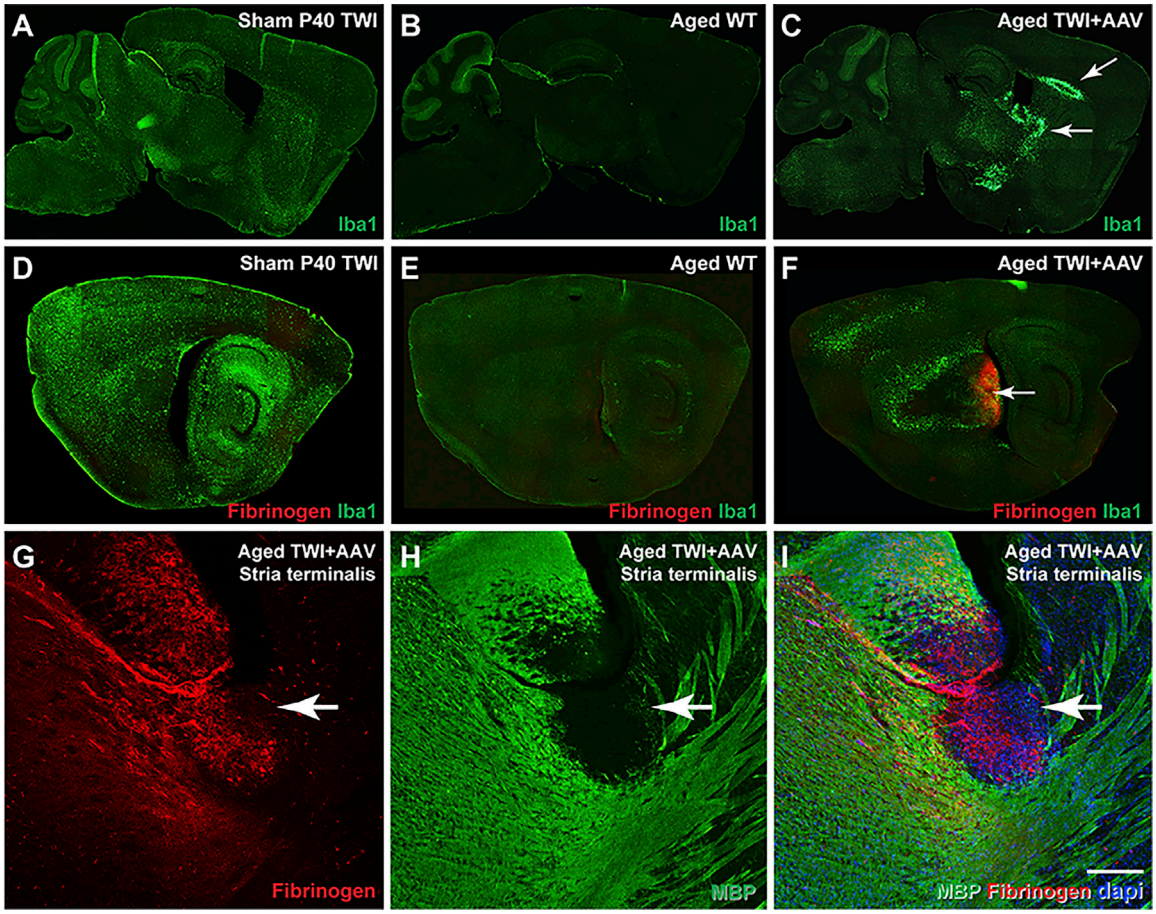

Figure 4. Lesions display evidence of microgliosis and plasma protein extravasation

(A–C) Tissue was stained with IBA1 to examine microglia, which revealed extensive microgliosis in the lesioned areas (C, arrows) in contrast to extensive, global microgliosis in sham TWI (A) and minimal microglia in aged WT (B). (D–F) Tissues were double stained for fibrinogen and IBA1, which showed that fibrinogen leakage was limited to the lesioned regions in aged TWI+AAV (F) and colocalized with IBA1 staining. No fibrinogen leakage was observed in sham TWI (D) or aged WT (E). (G–I) Aged TWI+AAV were double stained for fibrinogen (G) and MBP (H) to depict how fibrinogen extravasation is present in the lesioned areas (I). Scale bars: (A–C)1.8 mm; (D–F)1.3 mm; (G–I) 100 μm.

activation of SMAD. Phospho-SMAD1 (pSMAD1) was significantly increased in the aged TWI+AAV brain (Figure 5W), in support of the involvement of this pathway.

Degradation of tight-junction components underlying the leakage of fibrinogen in adult-onset lesions

There is a direct correlation between the quantity of plasma proteins and other blood elements leaking in the brain parenchyma and the integrity and permeability of the BBB.[23] The efficiency of the BBB to prevent extravasation is largely regulated by the presence of tight junctions, which serve to fully seal the space between endothelial cells of the brain vasculature.[25,29] To evaluate the possibility that fibrinogen extravasation is associated with BBB discontinuity, we examined the integrity of the BBB with isolectin-fluorescein isothiocyanate (FITC) staining, which reliably detects disruptions in the continuity of the BBB (Figures 6A–6F). Our results clearly show that within the lesioned areas of the aged, treated TWI, the vessel walls have discontinuities (Figures 6E and 6F, arrowheads). In contrast, non-lesioned areas of the aged, treated TWI brains (Figure 6D, arrows) and P40 TWI+AAV (Figure 6C, arrows) showed a smooth and continuous staining, indistinguishable from WT vessels (Figure 6B) and sham TWI (Figure 6A). Several protein components of the tight junction are sensitive to instability and degradation. Occludin and various claudin proteins play key scaffolding roles in tightening the BBB and can be targeted for degradation by matrix metalloproteinases such as MMP9.[34,35] To analyze whether the discontinuity of the vessel detected by isolectin labeling was accompanied by changes in tight junction components, we measured the levels of occludin, claudin5, and activated MMP9. A significant increase in the active form of MMP9 in protein lysates of aged TWI+AAV mice was identified (Figure 6G). A stark increase in the presence of the 60-kDa degraded form of occludin was readily observed in aged TWI lysates, statistically significant from degradation levels observed in any other conditions (Figure 6H). Similarly, levels of claudin5 were significantly reduced in aged TWI+AAV brains with respect to the levels in any of the other experimental conditions (Figure 6I).

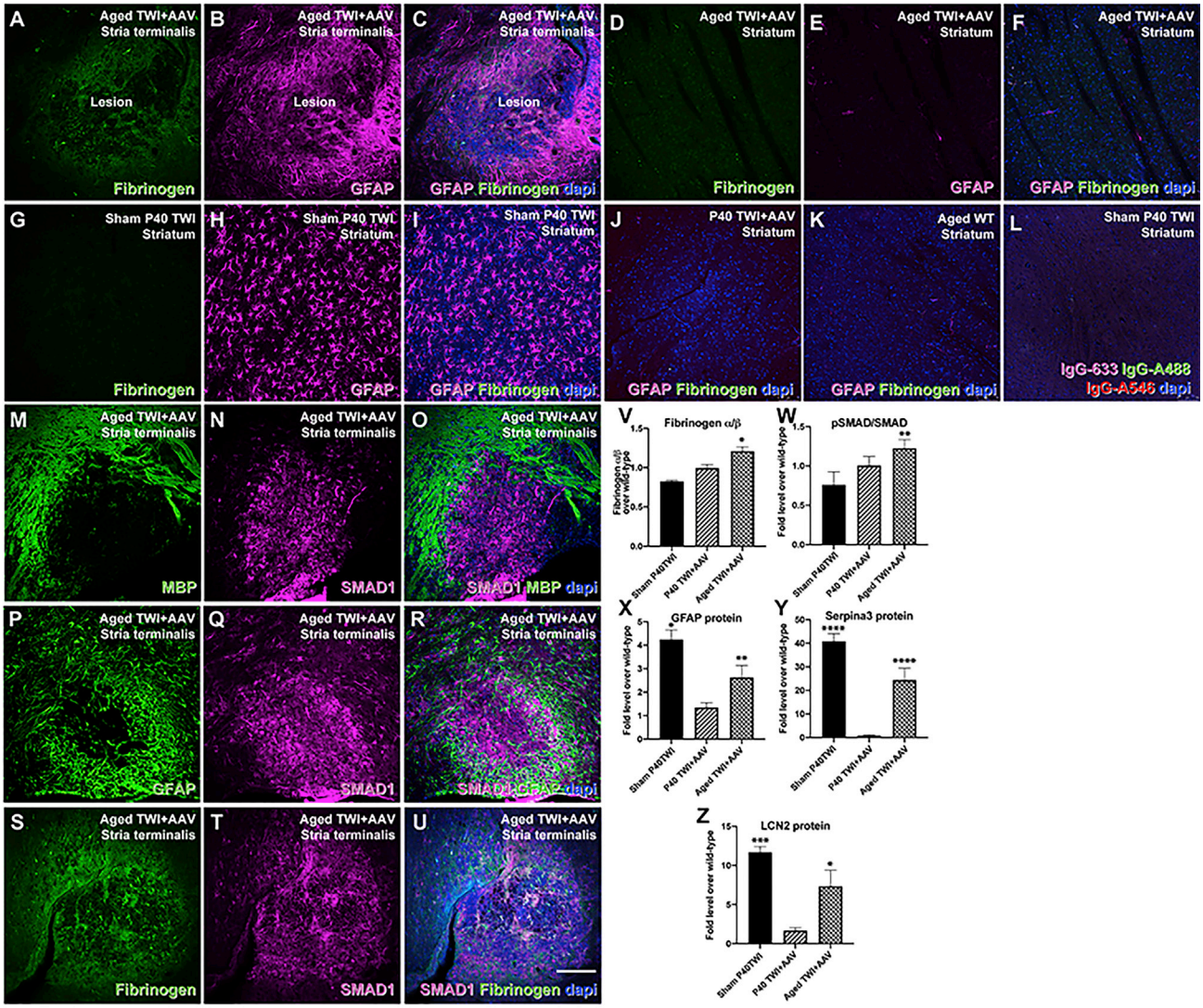

Figure 5. Areas with fibrinogen deposition present widespread astrogliosis

(A–C) Tissue sections double stained for fibrinogen (green) and GFAP (purple) showed strong colocalization of these proteins within the lesioned areas of aged TWI+AAV. (D–F, J, and K) In contrast, non-lesioned regions of aged TWI+AAC such as the striatum (D–F), P40 TWI+AAV (J), and aged WT (K) had undetectable fibrinogen and normalized expression of GFAP$^+$ astrocytes. (G–I) Sham P40 TWI showed no fibrinogen but extensive astrogliosis through the brain. (L) Background staining of secondary antibodies is shown. (M–O) Aged TWI+AAV tissue was double stained for MBP (M) and SMAD1 (N) revealing that SMAD1 expression was limited to the demyelinated lesions (O). (P–R) Likewise, robust expression of SMAD1 (Q) was associated with GFAP (P) in aged TWI+AAV tissue (R). (S–U) Tissue was double stained for fibrinogen (S) (green) and SMAD1 (T) (purple), again showing a strong colocalization within the lesions (U). (V–Z) Quantitative immunoblotting enabled the quantification of increased levels of fibrinogen—alpha subunit, (V), phosphorylated SMAD1 (W), GFAP (X), Serpina3 (Y), and LCN2 (Z). n = 3; *p ≤ 0.05, **p ≤ 0.01, ***p ≤ 0.001, ****p ≤ 0.0001. Scale bars: 100 μm.

Lesion-associated OPCs are depleted of detectable GALC: reemergence of GALC metabolic deficiency by exhaustion of the therapeutic AAV genome

Because oligodendrocytes are the main contributor to psychosine production in KD,[36] the recruitment of proliferating OPCs[37,38] lacking the therapeutic transgene to an area for damage (likely a doomed attempt to improve remyelination) could contribute to further psychosine accumulation, leading to additional damage. Based on these findings, we hypothesized that the proliferation of OPCs in the treated TWI brain dilutes the episomal AAV9-GALC plasmid,[39–43] rendering *de novo* OPCs with minimal to zero therapeutic GALC enzyme. Accordingly, these newly formed cells are expected to have limited, if any, lysosomal GALC activity to metabolize psychosine.[42] Upon transducing a cell, the DNA packaged within an AAV primarily forms extra-chromosomal, non-replicating episomes.[39–43] We hypothesized that the focal lesions occurred because of a localized loss of AAV9-GALC DNA leading to the loss of GALC and the resulting accumulation of psychosine. Multiple lines of

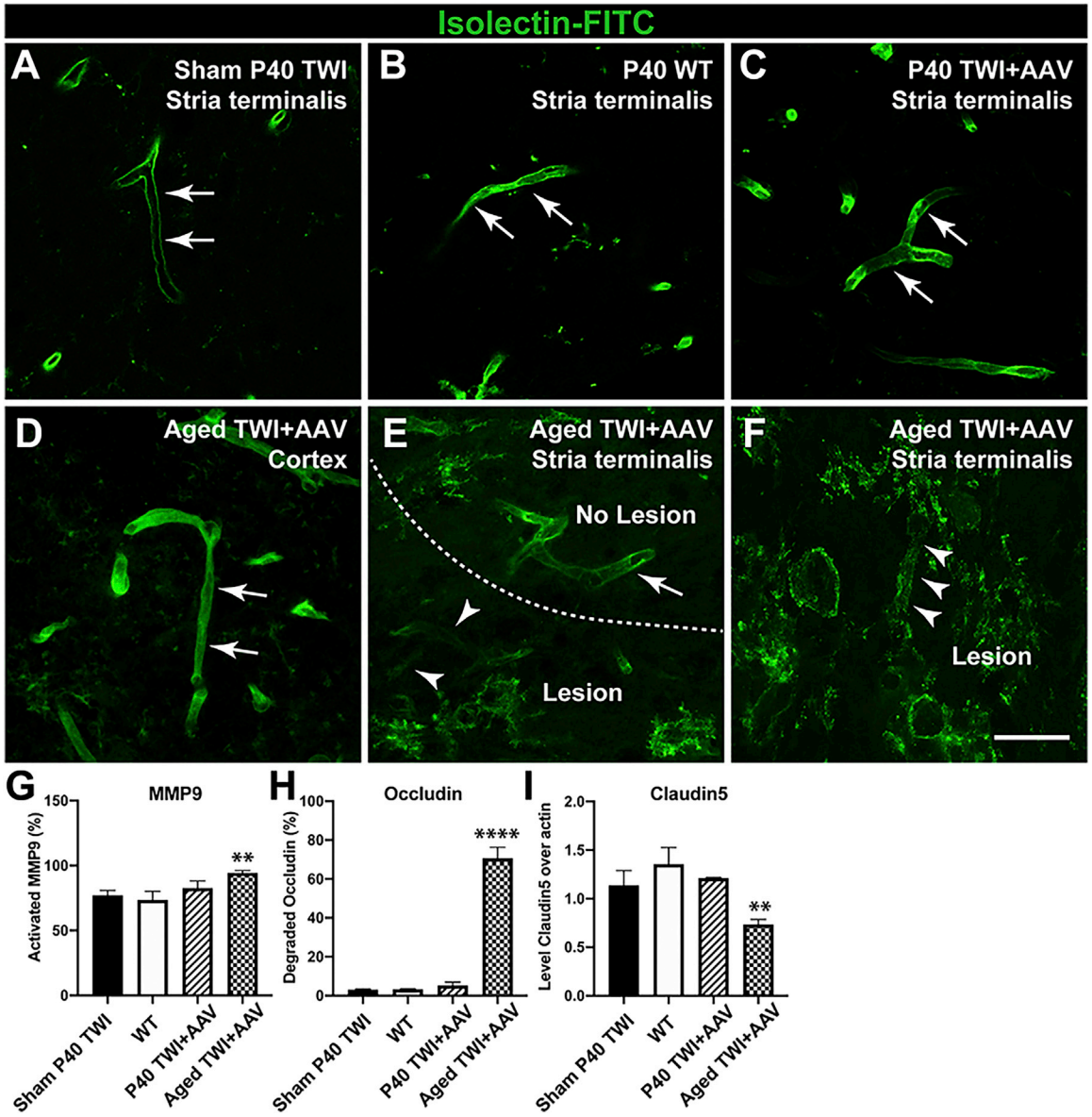

Figure 6. Degradation of endothelial tight junctions in blood vessels within lesions

(A–F) Tissue was stained with isolectin-FITC to examine the integrity of capillaries. (E–D) This showed that capillaries within aged TWI+AAV lesions (E and F) were damaged and disrupted in contrast to the non-lesioned areas such as the cortex (D). (A–C) The continuous staining observed in capillaries in sham P40 TWI (A), P40 WT (B), and P40 TWI+AAV (C) underscores the lack of vasculature disruption. (G–I) Immunoblotting enabled the quantification of changes in increased MMP9 (G), degradation of occludin (H), and reduction of claudin5 (I). n = 3; $^{**}p \leq 0.01$, $^{****}p \leq 0.0001$. Scale bars: 75 μm (A–F).

experimental evidence support this. We examined the expression of GALC protein in OPCs. Figure 7 shows that platelet-derived growth factor receptor-α^+ ($^{(}$PDGFR-α^+) OPCs (Figure 7B, arrows) found in lesioned areas of aged TWI+AAV are completely devoid of detectable levels of GALC (Figures 7A and 7C, arrows), similar to PDGFR-α^+ OPCs in sham TWI (Figures 7G–7I, arrows). Similar findings were observed in aged TWI+AAV+BMT (data not shown). Instead, PDGFRα^+ OPCs located in unaffected regions of the TWI brain such as cortex (Figure 7E, arrow) contained detectable levels of GALC (Figures 7D and 7F, arrow), similar to PDGFR-α^+ OPCs in WT (Figures 7J–7L, arrows).

Demyelinating lesions contain dividing oligodendrocyte progenitors

DAPI staining (Figures 8B–8E) revealed a hypercellular profile within lesions in comparison to WT (Figure 8A). Given the hypercellularity of these lesions, we examined these regions for the presence of dividing cells. For this, we used immunofluorescent

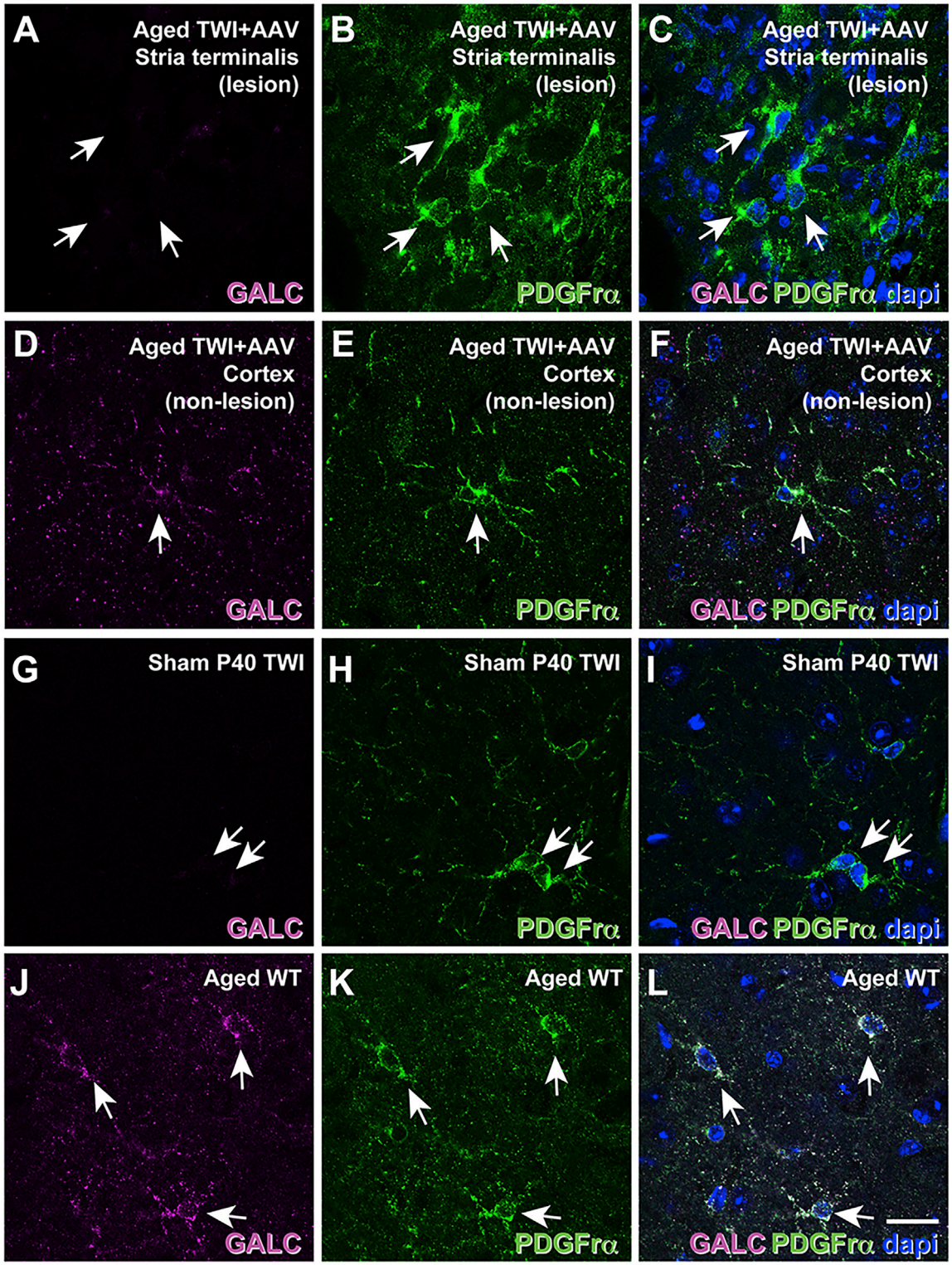

Figure 7. Loss of GALC transgenic expression in OPCs within lesions

Tissue was double-stained for GALC (purple) and PDGFR-α (green) to investigate the possibility of OPCs losing the GALC transgene in aged, treated TWI brains. (A–F) Confocal microscopy showed that OPCs within lesions of aged TWI+AAV (A–C, arrows) lacked detectable levels of GALC protein, while OPCs located outside lesioned areas such as the cortex (D–F, arrow) showed GALC expression. (J–L) Aged WT showed detectable GALC expression within OPCs (J–L, arrows), while sham P40 TWI showed a total absence of GALC expression within OPCs (G–I, arrows). Scale bars: 30 μm.

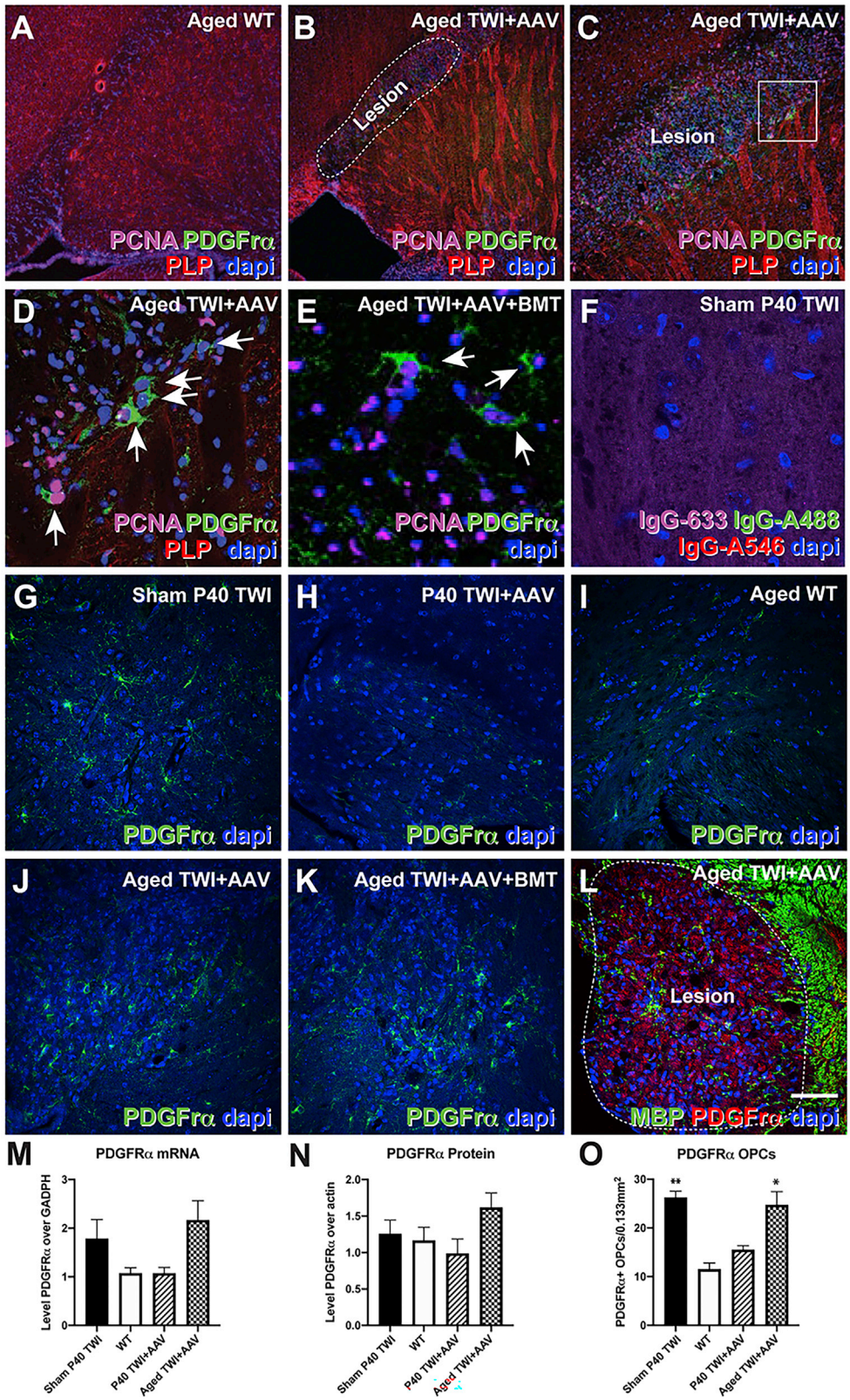

(legend on next page)

identification of proliferative cell nuclear antigen (PCNA)-positive nuclei. Abundant PCNA$^+$ nuclei were primarily concentrated around the margin and within the lesions, suggesting the lesions were active zones of cellular proliferation (Figures 8B–8E). Proliferation of OPCs has been shown to occur in the brain of TWI mice,[44] especially during the late stages of disease, as well as in the adult human brain.[45–47] To determine whether dividing OPCs made up a significant portion of the proliferative cells found in lesions, we co-stained brain sections with antibodies against PCNA and PDGFR-α, a well-characterized receptor expressed by replicating OPCs.[48] Our results confirmed the presence of abundant double-positive PDGFR-α/PCNA OPCs undergoing cell division within lesions (Figures 8B–8E, arrows). Secondary antibody controls are shown in Figure 8F. To quantify this response, we performed quantitative PCR (qPCR) for the *Pdgfrα* mRNA. Figure 8M shows that while P40 TWI+AAV mice have levels of *Pdgfrα* mRNA comparable to WT, the brain of aged TWI+AAV mice have an ∼2-fold increase in *Pdgfrα* mRNA expression. Western blot analysis shows similar changes in the levels of PDGFR-α protein (Figure 8N). Finally, counting of the PDGFR-α$^+$ OPCs within the lesion areas (Figures 8G–8L) also showed increased levels of OPCs (Figure 8O) in the aged TWI+AAV brain in comparison to P40 TWI+AAV.

We tested our hypothesis by transducing TWI neuroglial progenitors with AAV9-GALC at a multiplicity of infection (MOI) of 5,000, which approximates the dosage used in our *in vivo* gene therapy of TWI mice.[7] Samples were taken every 4 days for the quantification of episomal DNA via qPCR, GALC activity using our fluorescent assay,[7] and psychosine using MS. The results revealed a decline in viral DNA over time (Figure 9A). GALC activity per cell rapidly declined as well, showing a statistically significant decrease in 4 days, and it was no longer statistically different from the untreated TWI control after 20 days (Figure 9C). The decrease in viral DNA and GALC activity was not due to cell death, as the cumulative cell count over time showed a rapid increase in cells (Figure 9B).

To assess whether the loss of GALC activity led to an increase in psychosine in TWI cells, we quantified psychosine by LC-MS/MS[7] and compared the levels between early (4–8 days post-infection, DPI) and late (16–20 DPI) time points. Our results show that a significant decrease in psychosine in AAV-treated cells is measurable at early time points (4–8 DPI). In contrast, psychosine levels in AAV-treated cells increased to levels statistically indistinguishable from untreated cells at later time points (16–20 DPI) (Figure 9D). These results support our hypothesis that non-replicating, episomal AAV DNA is gradually diluted as cells replicate, leading to the reemergence of psychosine accumulation in newly generated TWI cells.

Finally, we investigated whether a similar dilutional process occurred in the mouse brain, particularly during proliferation of OPCs. This was accomplished by transducing WT mice with AAV-001-GFP, which was engineered to preferentially target OPCs and oligodendrocytes.[49] Mice were analyzed for GFP fluorescence at 7, 30, and 60 days of age (Figure 9E). This revealed a statistically significant decline in GFP fluorescence over time from an average fluorescence of ∼43 fluorescent units (FUs) at P7 to ∼14 FUs at P60 (Figure 9E). The number of fluorescent cells was also quantified, which revealed no significant difference between all time points (Figure 9F). These results further support our hypothesis that the proliferation of progenitor cells in the brains of adult AAV9-GALC-treated TWI (Figure 4) facilitates the dilution of therapeutic AAV-GALC genomes (Figures 2 and 9) and leads to a progressive decrease in corrective levels of GALC activity with an increase in psychosine (Figures 2 and 9) and recapitulation of neuropathology in localized areas (Figure 1).

In summary, our study presents multipronged experimental evidence that adult-onset multifocal demyelinating inflammatory lesions linked to BBB disruption and extravasation of plasma fibrinogen form in the brains of neonatally AAV9-GALC- and AAV9-GALC+-BMT-treated TWI mice. Our study identifies the focal reemergence of GALC metabolic deficiency in treated TWI arising from the proliferation of OPCs leading to the loss of the episomal AAV DNA containing the therapeutic transgene.

DISCUSSION

AAV gene therapy is proving to be a viable and useful treatment option for monogenetic disorders such as KD. The efficacy of AAV vectors seems paramount if administrated in early infancy, lasting significant periods of time thereafter. Our published protocol[7] is an example of early intervention leading to an effective means of significantly extending the lifespan and delaying the onset of demyelination and inflammation, matching the efficacy of AAV therapies observed by other groups.[8,11–14,50] However, the dynamics of maintaining therapeutic levels of GALC correction during longer periods of time extending into adulthood are less clear. Here, we are the first to describe in detail an adult-onset presentation of KD pathology in long-surviving AAV-treated TWI mice as multi-focal demyelinating lesions with associated inflammatory cells and lysosomal dysfunction. These data are supported by the discovery of similar lesions in aged mice from an independent study performed by the Sands group.[14] Our work shows that these lesions are observed only in long-lived animals. Although many of the animals in this study surpassed survival benchmarks of some previous reports, it does not seem that longevity is a significant factor, as these lesions were identified as early as P180. The reason may also be secondary to the unique regimen of the protocol used, which included a global delivery (via i.c., i.t., and i.v. injections) of

Figure 8. Lesions display signs of active cellular replication with increased numbers of OPCs

(A–F) DAPI staining revealed hyper-cellularity in lesions in AAV9-GALC-treated TWI mice (B–E, dotted line) compared to WT (A), containing abundant proliferating PNCA$^+$, PDGFR-α$^+$ OPCs (D, arrows). Secondary antibody controls are shown in (F). (G–L and O) Tissue from sham P40 TWI (G), P40 TWI+AAV (H), aged WT (I), aged TWI+AAV (J and L), and aged TWI+AAV+BMT (K) were stained with antibodies against PDFGr-α to enable the counting of OPCs (displayed in O). (M) Quantitative PCR of PDGFR-α mRNA. (N) Western blot quantification of PDGFR-α protein. n = 3; *p < 0.05, **p < 0.01. Scale bars: 100 μm (A, B, and G–L); 75 μm (C); 30 μm (D–F).

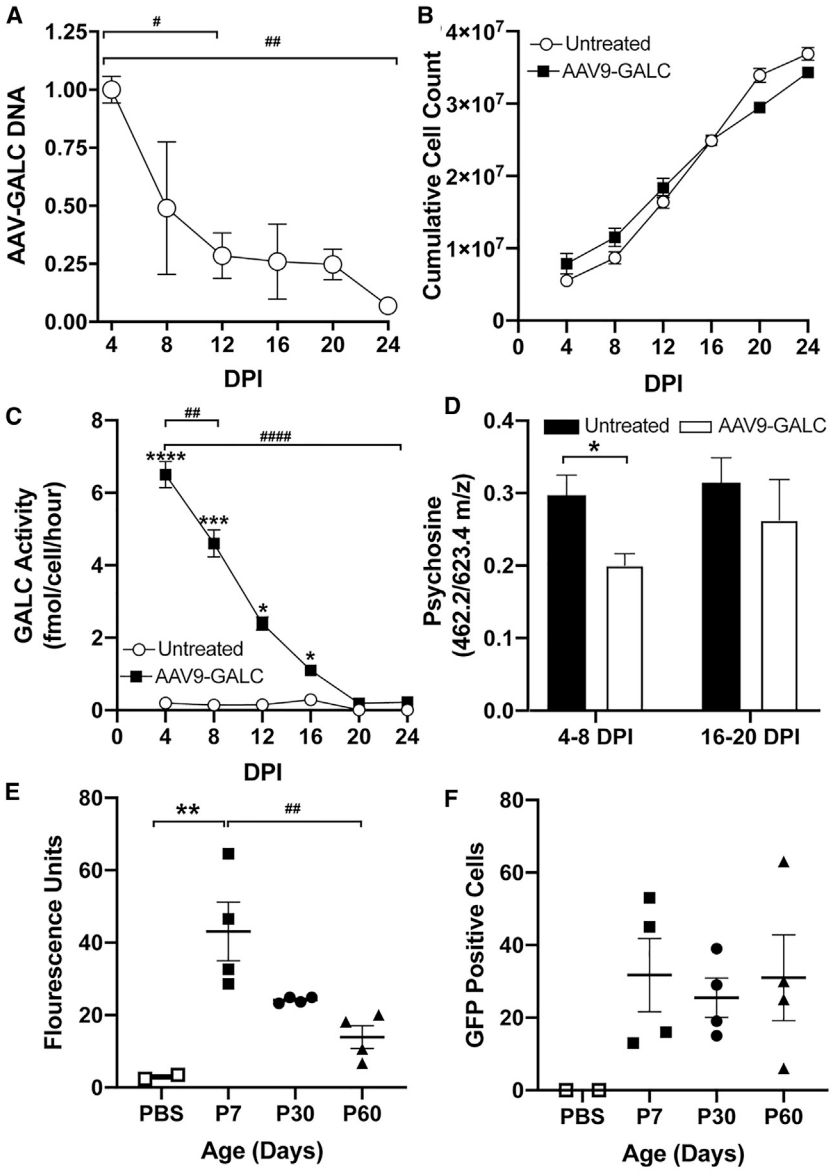

Figure 9. AAV DNA and transgene expression diminish *in vitro* and *in vivo* over time

(A–D) *In vitro*. (A–C) AAV-DNA (A) and GALC activity (C) per cell decreases over time in a manner inversely proportional to cumulative cell count (B). (D) LC-MS/MS quantification of psychosine shows that at early time points, 4–8 days post-infection (DPI), there was a significant reduction of psychosine after treatment with AAV9-GALC. Late time points, 16–20 DPI, show that there is no longer a significant difference between AAV9-GALC treated and untreated cells. (E and F) *In vivo* quantification of fluorescence intensity (E) of transduced cells in the brains of WT mice after transduction with AAV-001-GFP at 7, 30, and 60 days after injection. There is a significant decrease over time in AAV-001-GFP-mediated GFP fluorescence in mice brains. Counting the number of GFP^+ cells (F) revealed that the total number of transduced cells remains relatively constant. n = 3 for (A)–(D); n = 4 per time point for (E) and (F). The asterisk indicates the difference between groups and the # indicates the difference between time points. *p ≤ 0.05, **p ≤ 0.01, ****p ≤ 0.0001.

a higher titer AAV-GALC therapy regimen.[7,8,11,14] The widespread, high titer treatment could have resulted in greater initial correction, which may have hidden the local loss of GALC leading to the observed focal lesions.

Regional distribution of lesions in the brain does not appear to represent a limitation in the initial distribution of the vector as we confirmed GALC expression at P40 within the regions later affected by local demyelination. This idea is further supported by previous data that confirmed the AAV9-GFP vector to be present in all areas of the brain, and that there was no localized demyelination or neuroinflammatory phenotype observed in AAV9-GALC-treated animals at P40.[7] The mechanism responsible for initiating damage in these lesions, and therefore driving the regional specificity, could be related to local rates of myelin turnover, involving the generation of new oligodendrocytes. In fact, the proliferation of OPCs has been shown to occur in the TWI CNS[44] as well as in the adult human brain.[45–47] Myelination is a key driver of psychosine production,[51] suggesting that these regions may normally undergo increased myelin remodeling, with uncorrected OPCs acting as a potential trigger for damage as animals age. Other studies have presented evidence of regional differences in myelin quality,[52] which may be related to adult myelin remodeling following normal motor learning.[53] One anatomical region consistently affected by focal demyelination was the stria terminalis, directly adjacent to the subventricular zone, an area of permanent cell proliferation in the adult brain.[54]

This concentrated insult seems to reveal localized areas of myelin vulnerability and blood-brain/blood-cerebrospinal fluid barrier vulnerability, characterized by serum extravasation and fibrinogen leakage, which has been demonstrated to further activate microglia recruitment and axonal damage via a CD11b/CD18 mechanism.[27] The observation of plasma protein extravasation implies that there are deficits at the BBB (capillaries), the post-capillary venules, or the blood-cerebrospinal fluid barrier. Although the infiltration of hematogenous cells into the CNS of TWI has been reported,[55] leakage of plasma proteins has not been observed previously. In fact, the BBB had been shown to remain largely intact in the TWI,[56] suggesting the emergence of a new mechanism of damage in aged AAV9-GALC-treated TWI.

Because the AAV vector DNA exists largely as non-replicating extrachromosomal episomes, cellular proliferation inexorably causes its

progressive dilution by successive cell division, which decreases the average number of episomes per cell. The in *vitro* experiments demonstrated this by showing that episomal viral DNA and transgene encoded GALC declined over time, inversely proportional to cumulative cell count. This effect correlated to increases in psychosine levels, proportionally to cumulative cell count. The *in vivo* experiments provided further evidence of this effect by showing that fluorescent levels originating from AAV-encoded GFP decreased over time, despite the maintenance of the overall number of fluorescent cells over the duration of the experiment. Because fluorescence is proportional to the transgene expression levels, as transduced cells divide and dilute AAV genome, highly fluorescent cells become less fluorescent, to the point at which fluorescence is minimal or indistinguishable from background.

Given enough time, some cells may lose all copies of the therapeutic episomal *Galc* DNA, essentially reverting to an untreated state. Those cells and all progeny cells thereafter will be metabolically deficient in their ability to catabolize psychosine. The rapid loss of AAV DNA and GALC transgene per cell in transduced TWI neuroglial progenitors as well as the decline of AAV-mediated GFP fluorescence over time support this episome dilutional hypothesis. We speculate that this dilutional effect could explain the reduction of GALC activity and increased psychosine concentrations detected in TWI as the animals age, compared to levels observed at P40, as previously reported.[7] In the context of myelin remodeling, if newly generated TWI OPCs continue to increase the local levels of psychosine, this may activate repair mechanisms that direct newly formed cells to the site of injury.[21] Uncorrected repair/inflammatory cells (e.g., OPCs, astroglia, microglia), possessing a limited capacity to break down psychosine, likely enhance the local lesion into a demyelinated lesion. This is supported by the observed loss of *Galc* transcriptional expression and GALC protein within the lesions and, more important, in OPCs within the lesion, suggesting a cellular turnover with the invasion of non-corrected cell types.

Beyond an evaluation of the ability of an AAV vector to initially correct the pathophysiology of disease, our results provide an interesting observation for how a localized loss of lysosomal function can lead to a presentation that is reminiscent of other focal demyelination such as multiple sclerosis. Heterozygous *Galc* mutants have been shown to have reduced remyelination and clearance of myelin debris,[57,58] which supports our theory that the progressive loss of GALC increases myelin vulnerability in the adult and aging brain.

Our study has not fully addressed the temporal nature of how the lesions develop. At this time, we hypothesize that glial cells within the lesioned areas may naturally replicate faster than other regions of the CNS in response to myelin remodeling, leading to more rapid dilution of the therapeutic episomal transgene. This would explain why the lesions were only found within specific areas. Initially, these cells may be metabolically functional, aided by cross-correction from neighboring cells secreting GALC.[59–61] However, uncorrected cells, as well as an exponentially increasing number of initially corrected cells losing AAV episomal copies, reach a point at which psychosine burden from the uncorrected cells is too large for neighboring cells to correct and pathological effects emerge.[3,62–69] Cell death and debris result in astrogliosis, inflammation, and activation of microglia. Inflammatory cells are known to produce MMP9,[70–72] which participates in breakdown components of the BBB such as claudin5.[34,35] BBB failure allows the extravasation of blood components such as fibrinogen, which augments astrogliosis, inflammation, and generalized damage.

We did not observe signs of remyelination within the lesions on EM microscopy; however, this still leaves the question of whether these lesions progressively worsen or whether there may be periods of remission. Progressive lesions would be consistent with the proposed mechanism of episomal dilution and recruitment of uncorrected repair cells, no longer containing GALC protein, and would lead to a dysfunctional repair process. Further studies will address these aspects of the pathogenic mechanism.

The observations presented in this study hold important implications. Undoubtedly, the recent cascade of positive results using AAV gene therapy obtained in the KD mouse and GLD dog model[7,10–12,14,73] exemplifies the advantage of these vectors and supports their future use in clinical trials for KD. While this excitement is totally justified and is expected to gain further momentum, our study, along with recent findings of liver toxicity in AAV-treated TWI mice,[74] highlight the importance of studying long-term safety when using AAV gene therapy for CNS treatment. Further improvements in gene therapy reagents, delivery procedures, and quality control protocols will ensure more refined, efficient, long-lasting, and safer results for KD patients.

MATERIALS AND METHODS

Animals and therapy protocol

Animal work in this study was performed in accordance with approved protocols from the Animal Care and Use Committee at the University of Illinois at Chicago. WT ($Galc^{+/+}$) and TWI ($Galc^{-/-}$) mice were identified via PCR, as previously described,[75] all maintained on a C57BL/6J background. Males and females were both used in this study and randomly distributed as treatment was initiated before the sex could be identified.

Neonatal TWI mice (P0–P1) were treated with AAV9-GALC via three delivery routes—i.c., i.t., and i.v.— at a dosage of 9.0×10^9 vg in 5×1 μL PBS, 8.25×10^{10} vg in 18 μL PBS, and 3.3×10^{11} vg in 30 μL PBS, respectively (4.2×10^{11} vg total, indicated as TWI+AAV). i.t. injections were performed with a 28-G insulin syringe (4428-1, Jelco/Smiths Medical ASD, Keene, NH, USA), inserted between L5 and S1, with 1% trypan blue added to the solution for tracing. i.v. injections were delivered to the superficial temporal vein using a 28-G insulin syringe. i.t. and i.v. injections were performed with pups backlit by a red-light lamp to visualize the spinal cord and vein. i.c. injections were performed as 5 separate injections (1 μL each, 2 in the left cortical hemisphere, 2 in the right cortical hemisphere, and 1 in the cerebellum) with a 26-G Hamilton syringe Model #701 (Hamilton, Reno, NV, USA) inserted 1 mm into the brain parenchyma).

Neonatal (P1) WT C57BL/6J were transduced with AAV-001-GFP or PBS control at a dosage of 1.0×10^8 vg in 4×1 μL injections (bilateral cortex and thalamus) with a 26-G Hamilton syringe.

All of the injections were performed under isoflurane anesthesia, 1 h after a 2-mg/kg subcutaneous injection of meloxicam (Boehringer Ingelheim Vetmedica, St. Joseph, MO) for the treatment of post-procedure pain and inflammation. Povidone-iodine cat. no. 67618-155 (Betadine, Stamford, CT, USA) was applied to the skin to disinfect before injections.

After 24 h of recovery, a subset of AAV9-GALC treated mice (indicated as TWI+AAV+BMT) were given an additional i.v. treatment of bone marrow stem cells harvested from 6- to 8-week-old syngeneic WT mice (30 million cells each treatment). Bone marrow cells were harvested by flushing the tibiae and femur bones, pelleting the cells, and then resuspending in Dulbecco's modified Eagle's medium cat. no. 11966 (Thermo Fisher Scientific, Waltham, MA, USA). An additional control group of TWI mice was treated only with bone marrow on P2 (TWI+BMT only). To measure BMT engraftment efficiency, a subset of mice received bone marrow from C57BL/6J background mice expressing ECFP fluorescent cells (mouse stock no. 004218, The Jackson Laboratory, Bar Harbor, ME, USA). A group of sham (sterile PBS) i.t., i.v., and i.c. injections on TWI and WT were also performed at P1–P2 days of age. After the treatments, the mice were returned to their home cage with their mother.

Quantification of locomotor ability and tremor

Beginning on P20, animals had their locomotor capabilities and tremor quantified twice per week until 20 weeks and once per week thereafter. Quantification was performed by the same blinded observer every session. Locomotor ability was scored as follows: normal, 0; waddling, 1; partial paralysis, 1.5; and full paralysis, 2. Tremor was scored in a binary system of no tremor, 0 and tremor present,1.

Vector design and production

The AAV9-GALC vector was made using an inverted terminal repeat (ITR) plasmid provided by Mark Sands' laboratory at Washington University in St. Louis, with the Chicken-Beta Actin (CBA-CAGGS) promoter driving murine *Galc*, as described.[50] The AAV9.47-GFP vector was produced using a plasmid encoding EGFP, driven by the CBh promoter,[76] along with a SV40 poly A tail. These were packaged as single-stranded genomes in an AAV capsid.

The AAV-001-GFP vector was made by the directed evolution of AAV1, AAV2, AAV2i8, AAV2.5, AAV6, AAV8, AAV9, AAV9.47, and AAVrh10 capsids. The capsid library was introduced to rats given 6-hydroxy-dopamine and then recovered via PCR. It contains an enhanced GFP transgene under the hybrid CBh packaged with a self-complementary genome,[49] which was generously provided to us by Dr. Stephen Gray.

Recombinant AAV vectors were generated by the triple transfection of suspension HEK293 cells, using methods developed at the University of North Carolina (UNC) Gene Therapy Center Vector Core facility (Chapel Hill, NC).[77] Vectors were dialyzed in phosphate-buffered saline (PBS) containing 5% D-sorbitol and 350 mM NaCl.

Psychosine quantification

Fresh tissue was homogenized in H_2O using a Vibra-cell ultrasonic liquid processor model no. VCX 130 (Sonics and Materials, Newton, CT, USA). Psychosine was extracted from tissue homogenates (200 μg) via a methanol-acetic acid solution (0.5% acetic acid in methanol). Using D-lactosyl-β1-1′-D-*erythro*-sphingosine cat. no. 860542P (Avanti Polar Lipids, Alabaster, AL, USA) as an internal standard, psychosine content was determined using MS/MS.

Chromatography

Separations were carried out using a Shimadzu (Kyoto, Japan) Nexera ultra-high-performance liquid chromatography (UHPLC) system equipped with a Waters (Milford, MA) Acquity UPLC BEH amide column (2.1 × 50 mm, 1.7 μm) or an Agilent (Santa Clara, CA, USA) 1290 Infinity II system equipped with a Poroshell 120 EC-C18 UHPLC column (2.1 × 100 mm, 2.7 μm). Psychosine was eluted from the ethylene bridged hybrid (BEH) amide column using a 30-s isocratic flow of 85% acetonitrile and 15% 5 mM ammonium formate and 0.2% formic acid in water at a flow rate of 0.90 mL/min. The injection volume was 1 μL, and the column temperature was 45°C. Data acquisition and integration were carried out using Shimadzu Lab Solutions software. Psychosine was eluted from the Poroshell 120 EC-C18 column using a gradient elution with mobile phases consisting of solvent (A) water + 0.1% formic acid (B) acetonitrile + 0.1% formic acid, and the flow rate was maintained at 0.3 mL/min. LC gradient was as follows: 0–3.5 min held at 86% (B); 3.5–4 min (B) was increased from 86% to 100%; 4–10 min held at 100% (B). Injection volume is 15 μL, and the column was maintained at 40°C.

Psychosine detection

The Agilent 1290 Infinity II UHPLC system was interfaced to an Agilent 6550 quadrupole time-of-flight mass spectrometer equipped with electrospray source, and the data were acquired in positive ion mode. Source parameters were as follows: nitrogen gas temperature (200°C), drying gas flow (12 L/min), nebulizer (35 psi), sheath gas temperature (350°C), sheath gas flow (11 L/min), VCap (3,500 V), nozzle voltage (500 V), and fragmentor voltage (130 V). MS and MS/MS *m/z* ranges were set to 50–1,700 with fixed collision energies of 25 eV. MS and MS/MS scan rates were 3 spectra per second. Data acquisition and integration were carried out using Agilent MassHunter software. A surrogate standard of D-lactosyl-β1-1′-D-*erythro*-sphingosine was used for relative quantification.

MS/MS

The Shimadzu Nexera UHPLC system was interfaced to a Shimadzu LCMS-8050 triple quadrupole mass spectrometer equipped with positive ion electrospray and operated at unit resolution. Nitrogen was used for nebulization at a flow rate of 3.0 L/min, drying gas at 10 L/min, and heating gas flow at 10 L/min. The ion source capillary and vaporizer temperatures were 300°C. Psychosine was measured

using collision-induced dissociation and selected reaction monitoring (SRM). Argon was used as the collision gas at a pressure of 230 kPa. The SRM transition for psychosine was *m/z* 462–282 and the transition for the surrogate standard D-lactosyl-β1-1′-D-*erythro*-sphingosine was *m/z* 624–282. The SRM dwell time was 50 ms.

GALC activity quantification

GALC activity was quantified as described previously.[7] Lysate was incubated with the GALC substrate cat. no. EH05989 (6HMU-β-D-galactoside, Carbosynth, Berkshire, UK) at 37°C for 17 h. Enzymatic activity was quantified via fluorescence on a DTX 880 Multimode Detector (Beckman Coulter, Brea, CA, USA) with 385 nm excitation and 450 nm emission.

ISH

FISH was performed on frozen brain sections with a *GALC* antisense FITC-riboprobe prepared by *in vitro* reverse transcription using a template derived from a 1.1-kb fragment of *Galc*. Briefly, the *Galc* probe used for ISH was generated by sub-cloning a 1.1-kb BamHI/XbaI piece of the 5′ end of the murine *GALC* cDNA from pBRLsin-PPT.hPGK mGALC-HA.Wrpe[78] into the PGEM plasmid. Sections were permeabilized by treatment with Proteinase K (1 μg/mL) for 20 min. After post-hybridization washes, bound FITC was detected with a peroxidase-conjugated anti-FITC antibody (PerkinElmer, Waltham, MA, USA) and incubation with the peroxidase substrate FITC-tyramide.[79] Following inactivation at 70°C, MBP immunohistochemistry was performed afterward, as previously described.[7] Fluorescence images were acquired using a Leica (Allendale, NJ, USA) DM5500 TC confocal microscope.

Immunofluorescence

Mice were anesthetized and perfused with saline, followed by fixation with 4% paraformaldehyde, before the tissue was processed for cryosectioning. Cryosections of 30 μm were blocked free-floating with blocking buffer (0.3 M glycine, 1% BSA, 5% normal donkey serum, 5% normal goat serum, 0.30% Triton X-100, Tris-buffered saline [TBS]) for 1 h at room temperature, followed by primary antibody incubation at 4°C in blocking buffer for 24–72 h. After washing with TBS, tissue was incubated with secondary antibodies at room temperature for 1 h in blocking solution and washed again in TBS. Tissue was mounted with Prolong Gold antifade reagent cat. no. P36931 (Life Technologies, Eugene, OR, USA). Primary antibodies used included the following: GFAP (mouse [Ms]) cat. no. MAB3402 (EMD Millipore, Darmstadt, Germany, 1:500 dilution), IBA1 (rabbit [Rb]) cat. no. 019-19741 (Wako Pure Chemical Industries, Osaka, Japan, 1:1,000 dilution), NeuN (Ms) cat. no. MAB377 (EMD Millipore, 1:500 dilution), APC/CC1 (Ms) cat. no. OP80-100UG (EMD Millipore, 1:50 dilution), P0 (chicken [Ck]) cat. no. PZ0 (Aves Labs, Tigard, OR, USA, 1:250 dilution), MBP (rat [Rt]) cat. no. MAB386 (EMD Millipore, 1:100 dilution), LAMP1 (Rt) cat. no. sc-19992 (Santa Cruz Laboratories, Santa Cruz, CA, USA, 1:300 dilution) PDGFR-α (Rb) cat. no. SC338 (Santa Cruz Biotechnology, Dallas, TX, USA, 1:200 dilution), PCNA (Ms) cat. no. SC56 (Santa Cruz Biotechnology, 1:500 dilution), Fibrinogen (Rb) cat. no. A0080 (Agilent-Dako, Santa Clara, CA, USA, 1:200 dilution), PLP (Rt) (AA3 monoclocal hybridoma, 1:100 dilution), and isolectin-FITC cat. no. L32478 (Thermo Fisher, 1:500 dilution). Secondary antibodies included the following: Alexa Fluor 488 Anti-Mouse cat. no. A-11029 (Thermo Fisher Scientific, 1:500 dilution), Dylight 488 Anti-Rabbit cat. no. 211-482-171 (Jackson ImmunoResearch, West Grove, PA, USA, 1:500 dilution), Cy3 Anti-Rabbit cat. no. 711-166-152 (Jackson ImmunoResearch, 1:500 dilution), Alexa Fluor 546 Anti-Mouse cat. no. A11030 (Thermo Fisher Scientific, 1:500 dilution), Dylight 549 Anti-Chicken cat. no. 003-500-003 (Jackson ImmunoResearch, 1:500 dilution), Alexa Fluor 647 Anti-Mouse cat. no. A21236 (Thermo Fisher Scientific, 1:500 dilution), and Dylight 649 Anti-Rabbit cat. no. 211-492-171 (Jackson ImmunoResearch, 1:500 dilution). Cell nuclei were stained with DAPI cat. no. D1306 (Thermo Fisher, 1:3,000 dilution in TBS). Immunofluorescent complexes were visualized using a Leica TCS SPE confocal laser with an upright DM5500Q Microscope (Leica Biosystems, Buffalo Grove, IL, USA).

Immunoblotting

Tissue was homogenized in 10 volumes of RIPA buffer cat. no. BP-115x (Boston BioProducts, Ashland, MA, USA) using a Vibracell ultrasonic liquid processor model number VCX 130 (Sonics and Materials). Lysates were incubated at 4°C with rocking for 1 h and then spun at 14,000 × *g* for 20 min. The supernatant was removed, and its protein concentration quantified via a BCA assay cat. no. 23225 (Thermo Fisher Scientific). A total of 12.5 μg protein lysate was loaded into 10-well 4%–12% Bis-Tris Protein Gels, 1.5 mm, cat. no. NP0335BOX (Thermo Fisher Scientific). After gel electrophoresis, protein transfer was made onto a polyvinylidene fluoride (PVDF) membrane cat. no. 1620177 (Bio-Rad, Hercules, CA, USA). Membranes were blocked with 5% milk/1% BSA in TBS-Tween (0.5%) (TBS-T) for 1 h at room temperature. Primary antibodies were diluted in 1% BSA/TBS-T and incubated at 4°C overnight. Secondary antibodies were diluted in 5% milk/TBS-T and incubated on blot for 1 h at room temperature. Blots were visualized with ECL reagent cat. no. 32106 (Thermo Fisher Scientific) on an Odyssey Fc Imaging system (LI-COR, Lincoln, NE, USA). Primary antibodies used included the following: actin (Rb) cat. no. A2066 (Sigma-Aldrich, St. Louis, MO, USA, 1:1,000 dilution), LAMP1 (Rat) cat. no. sc-199992 (Santa Cruz Laboratories, 1:500 dilution); PDGFR-α (Rb) cat. no. SC338 (Santa Cruz Biotechnology, 1:200 dilution), fibrinogen (Rb) cat. no. A0080 (Agilent-Dako, 1:200 dilution), Serpina3 (Goat) cat. no. AF4709 (R&D Systems, Minneapolis, MN, USA, 1:500 dilution), LCN2 (goat) cat. no. AF1857 (R&D Systems, 1:500 dilution); phosphoSMAD (Rb) cat. no. 06-702 (Upstate Biotechnology, Lake Placid, NY, USA, 1:500 dilution); SMAD (Mo) cat. no. 05-1459 (EMD Millipore, 1:200), MMP9 (Mo) cat. no. sc-393859 (Santa Cruz Biotechnology, 1:500 dilution); occludin (Mo) cat. no. 33-1500 (Thermo Fisher, 1:500 dilution); and claudin5 (Rb) cat. no. SAB4502981 (EMD Millipore, 1:500 dilution).

Neuroglial cell culture and collection

P1–P5 TWI mice were anesthetized with 400 mg/kg tribromoethanol before euthanasia. Neuroglial cells were isolated from the

subventricular zone and hippocampus of P1–P5 TWI pups and put into Earle's Balanced Salt Solution (EBSS) cat. no. E6267 (Sigma-Aldrich) containing 1 mg/mL papain cat. no. LS003126 (Worthington Biochemical, Lakewood, NJ, USA), 0.2 mg/mL L-cysteine cat. no. C7602 (Sigma-Aldrich), 0.2 mg/mL EDTA cat. no. 15575-038 (Life Technologies), and 0.2 mg/mL DNase cat. no. L5002007 (Worthington Biochemical) and incubated at 37°C for 45 min with gentle rocking. Cells were then centrifuged at 123 × *g* for 10 min and the supernatant removed. Cells were resuspended in GIBCO Hank's Balanced Salt Solution (HBSS) cat. no. 13170-112 (Thermo Fisher Scientific) with 100 U/mL GIBCO penicillin/streptomycin cat. no. 15140122 (Thermo Fisher Scientific) and 0.6% glucose and mechanically dissociated by repeat pipetting. For proliferation, neuroglial cells were grown in Neurocult Basal Medium (Mo and Rat) cat. no. 05700 (Stem Cell Technologies, Vancouver, BC, Canada) with Neurocult Proliferation Supplement (Mo and Rat) cat. no. 05701 supplement (Stem Cell Technologies) and 100 U/mL penicillin/streptomycin, 20 ng/mL human epidermal growth factor cat. no. AF-100-15 (PeproTech, Rocky Hill, NJ, USA, 10 ng/mL), 20 ng/mL human fibroblast growth factor cat. no. 100-18B (PeproTech, 10 ng/mL), and 1 μg/mL heparin cat. no. H3393 (Sigma-Aldrich). Neuroglial cells were cultured at 37°C, 5% CO_2, with daily perturbation to maintain single-cell suspension. Cells were counted on a hemocytometer before transduction with AAV9-GALC at a MOI of 5,000 vg/cell. Samples were collected every 4 days by centrifugation at 800 × *g* at 4°C for 10 min following resuspension in 100 μL H_2O for qPCR or H_2O with 1× protease and phosphatase inhibitor cat. no. 539134 (EMD Millipore) and cat. no. 524625 (EMD Millipore), respectively, for GALC activity quantification. Samples were then lysed using a VC 130 Vibra-cell ultrasonic liquid processor (Sonics and Materials).

DNA isolation and quantitative polymerase chain reaction (qPCR)

An equivalent volume of (25:24:1) phenol/chloroform/isoamyl alcohol (Invitrogen [Carlsbad, CA, USA] 1857C038, 4C #3) was added to the cell lysate before vortexing for 10 s. Samples were then centrifuged at 10,000 × *g* at room temperature for 30 s. The aqueous phase was transferred to a new tube and 1/10 volume of 3 M sodium acetate, pH 5.2, was added before vortexing. A 2× volume of ice-cold 100% ethanol was added and vortexed before placing on dry ice for 5 min. Samples were centrifuged at 15,000 × *g* at room temperature for 5 min and the supernatant removed. Room temperature 70% ethanol, 1 mL, was added before vortexing and centrifugation at 15,000 × *g* at room temperature for 5 min. The supernatant was discarded and samples were air dried for 15 min to allow any remaining ethanol to evaporate. The samples were resuspended in 50 μL TE buffer and quantified on a Nanodrop ND-1000 spectrophotometer (Thermo Fisher Scientific). 96-Well Clear PCR plates cat. no. MLL9601 were filled with 10 μL iTaq Universal SYBR Green Supermix cat. no. 172512 (BioRad), 0.4 μL 10 μM forward primer, 0.4 μL 10 μM reverse primer, 3 μL 20 ng/μL DNA, and 6.2 μL H_2O. AAV primers are as follows: forward 5′-TTGCTCTGACTGATGGCTTG-3′ and reverse 5′-CCACACCTGCAGCTCTTGTA-3′. Glyceraldehyde 3-phosphate dehydrogenase (GAPDH) primers are as follows: forward 5′-CATCACTGCCACCCAGAAGACTG-3′ and reverse 5′-ATGCCAGTGAGCTTCCCGTTCAG-3′. qPCR was performed on a CFX Connect Real Time PCR Optics Module (BioRad) with the following settings: 95°C for 2 min, then 40 cycles of 95°C for 10 s, then 50.3°C for 30 s, and ending with a gradual increase from 65°C to 95°C.

GFP fluorescence quantification

Animals were anesthetized perfused with saline followed by post-fixing brains in PBS with 4% paraformaldehyde (PFA) for 48 h. Brains were then cryosectioned at 30 μm on a SM2010R sliding microtome (Leica Biosystems). Tile-scanned images were taken on a LSM 880 confocal microscope with 20 air objective lens (Carl Zeiss AG, Jena, Germany). Collection parameters were as follows: excitation at 488 nm from an argon laser, 4% laser power, and 2.8 μm thickness. Every other section from each animal was analyzed to find the section with the highest fluorescence for comparison. The images with the highest fluorescence were then quantified in ImageJ (National Institutes of Health [NIH], Bethesda, MD, USA).

Electron microscopy

Animals were anesthetized before perfusion with heparinized PBS (0.09 mg/mL) and tissue was then removed and fixed with 3% paraformaldehyde/2% glutaraldehyde in 0.1 M cacodylate buffer (pH 7.4) for 12 h at 4°C. The tissue was then transferred to 4% paraformaldehyde/1% glutaraldehyde in 0.1 M cacodylate buffer (pH 7.4) until processed for EM. For EM, the tissue was embedded in araldite, and ultrathin sections prepared and stained as described.[80]

Statistical analysis

Statistics and graphs were prepared with Prism 8 software (GraphPad Software, La Jolla, CA, USA). Data were analyzed using a one-way ANOVA with a Tukey's post hoc analysis, with $p < 0.05$ considered significant. Graphs represent the mean of independent measurements with error bars representing the standard error of the mean. All immunoblotting was performed with technical replicates of at least 3. Variation was comparable between groups.

SUPPLEMENTAL INFORMATION

Supplemental Information can be found online at https://doi.org/10.1016/j.ymthe.2021.01.026.

ACKNOWLEDGMENTS

We thank Dr Steve Gray for the generous gift of the AAV-001-GFP vector and the technical assistance of Benas Jakobauskas, Monika Stoskute, and Alexandra Socovich. M.S.M. was funded through a pre-doctoral NRSA fellowship from the NIH (NRSA F30NS090684). E.R.B. was funded with grants from the NIH (R01 NS065808), the Legacy of Angels Foundation, Partners for Krabbe Disease Research, and the European Leukodystrophy Association.

AUTHOR CONTRIBUTIONS

G.J.H., M.S.M., and E.R.B. designed the study and analyzed the data; G.J.H. and M.S.M. administered all of the treatments; M.S.M. and

D.N. took care of the mouse colony; G.J.H., M.S.M., Y.I., and J.N.M. collected the tissue; M.S.M. prepared the psychosine extractions; K.C.P., S.M.C., E.R., and R.B.v.B. performed the MS measurements and the analysis of the psychosine concentrations; G.J.H., M.S.M., Y.I., J.N.M., L.M.T., and E.R.B. performed all of the histological staining and confocal and epifluorescent microscopy imaging; E.R.B. performed the EM imaging and analysis; M.I.G. and S.J.C. performed the immunoblotting; M.S.S. performed the independent quality control experiments for lesions at Washington University in St. Louis; G.J.H. cultured the neuroglial cells and performed qPCR as well as quantified the GALC activity on the lysates; G.J.H., M.S.M., and E.R.B. prepared the figures; G.J.H., M.S.M., and E.R.B. wrote the manuscript, with contributions from L.M.T., S.M.C., S.J.C., M.S.S., and M.I.G. All of the authors read and approved the manuscript.

DECLARATION OF INTERESTS

E.R.B. is a consultant for Lysosomal Therapeutics, E-Scape Bio, Gain Therapeutics, Affinia Therapeutics, and Neurogene. None of these entities participated in or contributed financially or intellectually to this work and the decision to publish.

REFERENCES

1. Suzuki, K., and Suzuki, Y. (1971). Krabbe's globoid cell leukodystrophy: deficiency of galactocerebroside beta-galactosidase activity. J. Neuropathol. Exp. Neurol. *30*, 145.
2. Svennerholm, L., Vanier, M.T., and Månsson, J.E. (1980). Krabbe disease: a galactosylsphingosine (psychosine) lipidosis. J. Lipid Res. *21*, 53–64.
3. Igisu, H., and Suzuki, K. (1984). Progressive accumulation of toxic metabolite in a genetic leukodystrophy. Science *224*, 753–755.
4. Suzuki, K., Tanaka, H., Yamanaka, T., and Van Damme, O. (1980). The specificity of beta-galactosidase in the degradation of gangliosides. Adv. Exp. Med. Biol. *125*, 307–318.
5. Krabbe, K. (1916). A new familial, infantile form of diffuse brain sclerosis. Brain *39*, 74–114.
6. Barczykowski, A.L., Foss, A.H., Duffner, P.K., Yan, L., and Carter, R.L. (2012). Death rates in the U.S. due to Krabbe disease and related leukodystrophy and lysosomal storage diseases. Am. J. Med. Genet. A. *158A*, 2835–2842.
7. Marshall, M.S., Issa, Y., Jakubauskas, B., Stoskute, M., Elackattu, V., Marshall, J.N., Bogue, W., Nguyen, D., Hauck, Z., Rue, E., et al. (2018). Long-Term Improvement of Neurological Signs and Metabolic Dysfunction in a Mouse Model of Krabbe's Disease after Global Gene Therapy. Mol. Ther. *26*, 874–889.
8. Rafi, M.A., Rao, H.Z., Luzi, P., and Wenger, D.A. (2015). Long-term Improvements in Lifespan and Pathology in CNS and PNS After BMT Plus One Intravenous Injection of AAVrh10-GALC in Twitcher Mice. Mol. Ther. *23*, 1681–1690.
9. Rafi, M.A., Rao, H.Z., Luzi, P., Luddi, A., Curtis, M.T., and Wenger, D.A. (2015). Intravenous injection of AAVrh10-GALC after the neonatal period in twitcher mice results in significant expression in the central and peripheral nervous systems and improvement of clinical features. Mol. Genet. Metab. *114*, 459–466.
10. Bradbury, A.M., Rafi, M.A., Bagel, J.H., Brisson, B.K., Marshall, M.S., Pesayco Salvador, J., Jiang, X., Swain, G.P., Prociuk, M.L., ODonnell, P.A., et al. (2018). AAVrh10 Gene Therapy Ameliorates Central and Peripheral Nervous System Disease in Canine Globoid Cell Leukodystrophy (Krabbe Disease). Hum. Gene Ther. *29*, 785–801.
11. Karumuthil-Melethil, S., Marshall, M.S., Heindel, C., Jakubauskas, B., Bongarzone, E.R., and Gray, S.J. (2016). Intrathecal administration of AAV/GALC vectors in 10-11-day-old twitcher mice improves survival and is enhanced by bone marrow transplant. J. Neurosci. Res. *94*, 1138–1151.
12. Qin, E.Y., Hawkins-Salsbury, J.A., Jiang, X., Reddy, A.S., Farber, N.B., Ory, D.S., and Sands, M.S. (2012). Bone marrow transplantation increases efficacy of central nervous system-directed enzyme replacement therapy in the murine model of globoid cell leukodystrophy. Mol. Genet. Metab. *107*, 186–196.
13. Reddy, A.S., Kim, J.H., Hawkins-Salsbury, J.A., Macauley, S.L., Tracy, E.T., Vogler, C.A., Han, X., Song, S.K., Wozniak, D.F., Fowler, S.C., et al. (2011). Bone marrow transplantation augments the effect of brain- and spinal cord-directed adeno-associated virus 2/5 gene therapy by altering inflammation in the murine model of globoid-cell leukodystrophy. J. Neurosci. *31*, 9945–9957.
14. Hawkins-Salsbury, J.A., Shea, L., Jiang, X., Hunter, D.A., Guzman, A.M., Reddy, A.S., Qin, E.Y., Li, Y., Gray, S.J., Ory, D.S., and Sands, M.S. (2015). Mechanism-based combination treatment dramatically increases therapeutic efficacy in murine globoid cell leukodystrophy. J. Neurosci. *35*, 6495–6505.
15. Ricca, A., Rufo, N., Ungari, S., Morena, F., Martino, S., Kulik, W., Alberizzi, V., Bolino, A., Bianchi, F., Del Carro, U., et al. (2015). Combined gene/cell therapies provide long-term and pervasive rescue of multiple pathological symptoms in a murine model of globoid cell leukodystrophy. Hum. Mol. Genet. *24*, 3372–3389.
16. Musolino, P.L., Lund, T.C., Pan, J., Escolar, M.L., Paker, A.M., Duncan, C.N., and Eichler, F.S. (2014). Hematopoietic stem cell transplantation in the leukodystrophies: a systematic review of the literature. Neuropediatrics *45*, 169–174.
17. Escolar, M.L., Poe, M.D., Martin, H.R., and Kurtzberg, J. (2006). A staging system for infantile Krabbe disease to predict outcome after unrelated umbilical cord blood transplantation. Pediatrics *118*, e879–e889.
18. Escolar, M.L., Poe, M.D., Provenzale, J.M., Richards, K.C., Allison, J., Wood, S., Wenger, D.A., Pietryga, D., Wall, D., Champagne, M., et al. (2005). Transplantation of umbilical-cord blood in babies with infantile Krabbe's disease. N. Engl. J. Med. *352*, 2069–2081.
19. Hildebrand, C. (1989). Myelin sheath remodelling in remyelinated rat sciatic nerve. J. Neurocytol. *18*, 285–294.
20. Sundaram, K.S., and Lev, M. (1985). Inhibition of cerebroside synthesis in the brains of mice treated with L-cycloserine. J. Lipid Res. *26*, 473–477.
21. Kondo, Y., Adams, J.M., Vanier, M.T., and Duncan, I.D. (2011). Macrophages counteract demyelination in a mouse model of globoid cell leukodystrophy. J. Neurosci. *31*, 3610–3624.
22. Gay, D., and Esiri, M. (1991). Blood-brain barrier damage in acute multiple sclerosis plaques. An immunocytological study. Brain *114* (Pt 1B), 557–572.
23. Ballabh, P., Braun, A., and Nedergaard, M. (2004). The blood-brain barrier: an overview: structure, regulation, and clinical implications. Neurobiol. Dis. *16*, 1–13.
24. del Zoppo, G.J., and Mabuchi, T. (2003). Cerebral microvessel responses to focal ischemia. J. Cereb. Blood Flow Metab. *23*, 879–894.
25. Kirk, J., Plumb, J., Mirakhur, M., and McQuaid, S. (2003). Tight junctional abnormality in multiple sclerosis white matter affects all calibres of vessel and is associated with blood-brain barrier leakage and active demyelination. J. Pathol. *201*, 319–327.
26. del Zoppo, G.J., and Milner, R. (2006). Integrin-matrix interactions in the cerebral microvasculature. Arterioscler. Thromb. Vasc. Biol. *26*, 1966–1975.
27. Davalos, D., Ryu, J.K., Merlini, M., Baeten, K.M., Le Moan, N., Petersen, M.A., Deerinck, T.J., Smirnoff, D.S., Bedard, C., Hakozaki, H., et al. (2012). Fibrinogen-induced perivascular microglial clustering is required for the development of axonal damage in neuroinflammation. Nat. Commun. *3*, 1227.
28. Ahn, H.J., Glickman, J.F., Poon, K.L., Zamolodchikov, D., Jno-Charles, O.C., Norris, E.H., and Strickland, S. (2014). A novel Aβ-fibrinogen interaction inhibitor rescues altered thrombosis and cognitive decline in Alzheimer's disease mice. J. Exp. Med. *211*, 1049–1062.
29. Vos, C.M., Geurts, J.J., Montagne, L., van Haastert, E.S., Bö, L., van der Valk, P., Barkhof, F., and de Vries, H.E. (2005). Blood-brain barrier alterations in both focal and diffuse abnormalities on postmortem MRI in multiple sclerosis. Neurobiol. Dis. *20*, 953–960.
30. Hamann, G.F., Okada, Y., and del Zoppo, G.J. (1996). Hemorrhagic transformation and microvascular integrity during focal cerebral ischemia/reperfusion. J. Cereb. Blood Flow Metab. *16*, 1373–1378.
31. Pous, L., Deshpande, S.S., Nath, S., Mezey, S., Malik, S.C., Schildge, S., Bohrer, C., Topp, K., Pfeifer, D., Fernández-Klett, F., et al. (2020). Fibrinogen induces neural stem cell differentiation into astrocytes in the subventricular zone via BMP signaling. Nat. Commun. *11*, 630.

32. Häggmark, A., Byström, S., Ayoglu, B., Qundos, U., Uhlén, M., Khademi, M., Olsson, T., Schwenk, J.M., and Nilsson, P. (2013). Antibody-based profiling of cerebrospinal fluid within multiple sclerosis. Proteomics *13*, 2256–2267.

33. Al Nimer, F., Elliott, C., Bergman, J., Khademi, M., Dring, A.M., Aeinehband, S., Bergenheim, T., Romme Christensen, J., Sellebjerg, F., Svenningsson, A., et al. (2016). Lipocalin-2 is increased in progressive multiple sclerosis and inhibits remyelination. Neurol. Neuroimmunol. Neuroinflamm. *3*, e191.

34. Spampinato, S.F., Merlo, S., Sano, Y., Kanda, T., and Sortino, M.A. (2017). Astrocytes contribute to Aβ-induced blood-brain barrier damage through activation of endothelial MMP9. J. Neurochem. *142*, 464–477.

35. Song, J., Hu, Y., Li, H., Huang, X., Zheng, H., Hu, Y., Wang, J., Jiang, X., Li, J., Yang, Z., et al. (2018). miR-1303 regulates BBB permeability and promotes CNS lesions following CA16 infections by directly targeting MMP9. Emerg. Microbes Infect. *7*, 155.

36. Schulte, S., and Stoffel, W. (1993). Ceramide UDPgalactosyltransferase from myelinating rat brain: purification, cloning, and expression. Proc. Natl. Acad. Sci. USA *90*, 10265–10269.

37. Keirstead, H.S., Levine, J.M., and Blakemore, W.F. (1998). Response of the oligodendrocyte progenitor cell population (defined by NG2 labelling) to demyelination of the adult spinal cord. Glia *22*, 161–170.

38. Reynolds, R., Cenci di Bello, I., Dawson, M., and Levine, J. (2001). The response of adult oligodendrocyte progenitors to demyelination in EAE. Prog. Brain Res. *132*, 165–174.

39. McCarty, D.M., Young, S.M., Jr., and Samulski, R.J. (2004). Integration of adeno-associated virus (AAV) and recombinant AAV vectors. Annu. Rev. Genet. *38*, 819–845.

40. Afione, S.A., Conrad, C.K., Kearns, W.G., Chunduru, S., Adams, R., Reynolds, T.C., Guggino, W.B., Cutting, G.R., Carter, B.J., and Flotte, T.R. (1996). In vivo model of adeno-associated virus vector persistence and rescue. J. Virol. *70*, 3235–3241.

41. Duan, D., Sharma, P., Yang, J., Yue, Y., Dudus, L., Zhang, Y., Fisher, K.J., and Engelhardt, J.F. (1998). Circular intermediates of recombinant adeno-associated virus have defined structural characteristics responsible for long-term episomal persistence in muscle tissue. J. Virol. *72*, 8568–8577.

42. Nakai, H., Yant, S.R., Storm, T.A., Fuess, S., Meuse, L., and Kay, M.A. (2001). Extrachromosomal recombinant adeno-associated virus vector genomes are primarily responsible for stable liver transduction in vivo. J. Virol. *75*, 6969–6976.

43. Schnepp, B.C., Jensen, R.L., Chen, C.L., Johnson, P.R., and Clark, K.R. (2005). Characterization of adeno-associated virus genomes isolated from human tissues. J. Virol. *79*, 14793–14803.

44. Taniike, M., and Suzuki, K. (1995). Proliferative capacity of oligodendrocytes in the demyelinating twitcher spinal cord. J. Neurosci. Res. *40*, 325–332.

45. Armstrong, R.C., Dorn, H.H., Kufta, C.V., Friedman, E., and Dubois-Dalcq, M.E. (1992). Pre-oligodendrocytes from adult human CNS. J. Neurosci. *12*, 1538–1547.

46. Duncan, I.D., Radcliff, A.B., Heidari, M., Kidd, G., August, B.K., and Wierenga, L.A. (2018). The adult oligodendrocyte can participate in remyelination. Proc. Natl. Acad. Sci. USA *115*, E11807–E11816.

47. Gogate, N., Verma, L., Zhou, J.M., Milward, E., Rusten, R., O'Connor, M., Kufta, C., Kim, J., Hudson, L., and Dubois-Dalcq, M. (1994). Plasticity in the adult human oligodendrocyte lineage. J. Neurosci. *14*, 4571–4587.

48. Hart, I.K., Richardson, W.D., Heldin, C.H., Westermark, B., and Raff, M.C. (1989). PDGF receptors on cells of the oligodendrocyte-type-2 astrocyte (O-2A) cell lineage. Development *105*, 595–603.

49. Powell, S.K., Khan, N., Parker, C.L., Samulski, R.J., Matsushima, G., Gray, S.J., and McCown, T.J. (2016). Characterization of a novel adeno-associated viral vector with preferential oligodendrocyte tropism. Gene Ther. *23*, 807–814.

50. Lin, D., Fantz, C.R., Levy, B., Rafi, M.A., Vogler, C., Wenger, D.A., and Sands, M.S. (2005). AAV2/5 vector expressing galactocerebrosidase ameliorates CNS disease in the murine model of globoid-cell leukodystrophy more efficiently than AAV2. Mol. Ther. *12*, 422–430.

51. Tanaka, K., Nagara, H., Kobayashi, T., and Goto, I. (1989). The twitcher mouse: accumulation of galactosylsphingosine and pathology of the central nervous system. Brain Res. *482*, 347–350.

52. Smith, M.E. (1973). A regional survey of myelin development: some compositional and metabolic aspects. J. Lipid Res. *14*, 541–551.

53. Xiao, L., Ohayon, D., McKenzie, I.A., Sinclair-Wilson, A., Wright, J.L., Fudge, A.D., Emery, B., Li, H., and Richardson, W.D. (2016). Rapid production of new oligodendrocytes is required in the earliest stages of motor-skill learning. Nat. Neurosci. *19*, 1210–1217.

54. Nait-Oumesmar, B., Decker, L., Lachapelle, F., Avellana-Adalid, V., Bachelin, C., and Baron-Van Evercooren, A. (1999). Progenitor cells of the adult mouse subventricular zone proliferate, migrate and differentiate into oligodendrocytes after demyelination. Eur. J. Neurosci. *11*, 4357–4366.

55. Wu, Y.P., Matsuda, J., Kubota, A., Suzuki, K., and Suzuki, K. (2000). Infiltration of hematogenous lineage cells into the demyelinating central nervous system of twitcher mice. J. Neuropathol. Exp. Neurol. *59*, 628–639.

56. Kondo, A., Nakano, T., and Suzuki, K. (1987). Blood-brain barrier permeability to horseradish peroxidase in twitcher and cuprizone-intoxicated mice. Brain Res. *425*, 186–190.

57. Scott-Hewitt, N.J., Folts, C.J., and Noble, M.D. (2018). Heterozygous carriers of galactocerebrosidase mutations that cause Krabbe disease have impaired microglial function and defective repair of myelin damage. Neural Regen. Res. *13*, 393–401.

58. Scott-Hewitt, N.J., Folts, C.J., Hogestyn, J.M., Piester, G., Mayer-Pröschel, M., and Noble, M.D. (2017). Heterozygote galactocerebrosidase (GALC) mutants have reduced remyelination and impaired myelin debris clearance following demyelinating injury. Hum. Mol. Genet. *26*, 2825–2837.

59. Scaravilli, F., and Suzuki, K. (1983). Enzyme replacement in grafted nerve of twitcher mouse. Nature *305*, 713–715.

60. Rafi, M.A., Fugaro, J., Amini, S., Luzi, P., de Gala, G., Victoria, T., Dubell, C., Shahinfar, M., and Wenger, D.A. (1996). Retroviral vector-mediated transfer of the galactocerebrosidase (GALC) cDNA leads to overexpression and transfer of GALC activity to neighboring cells. Biochem. Mol. Med. *58*, 142–150.

61. Luddi, A., Volterrani, M., Strazza, M., Smorlesi, A., Rafi, M.A., Datto, J., Wenger, D.A., and Costantino-Ceccarini, E. (2001). Retrovirus-mediated gene transfer and galactocerebrosidase uptake into twitcher glial cells results in appropriate localization and phenotype correction. Neurobiol. Dis. *8*, 600–610.

62. Taketomi, T., and Nishimura, K. (1964). Physiological Activity of Psychosine. Jpn. J. Exp. Med. *34*, 255–265.

63. Austin, J.H., and Lehfeldt, D. (1965). Studies in Globoid (Krabbe) Leukodystrophy. 3. Significance of Experimentally-Produced Globoid-Like Elements in Rat White Matter and Spleen. J. Neuropathol. Exp. Neurol. *24*, 265–289.

64. Miyatake, T., and Suzuki, K. (1972). Globoid cell leukodystrophy: additional deficiency of psychosine galactosidase. Biochem. Biophys. Res. Commun. *48*, 539–543.

65. Suzuki, K., Tanaka, H., and Suzuki, K. (1976). Studies on the pathogenesis of Krabbe's leukodystrophy: cellular reaction of the brain to exogenous galactosylsphingosine, monogalactosyl diglyceride, and lactosylceramide. Adv. Exp. Med. Biol. *68*, 99–114.

66. Taniike, M., Mohri, I., Eguchi, N., Irikura, D., Urade, Y., Okada, S., and Suzuki, K. (1999). An apoptotic depletion of oligodendrocytes in the twitcher, a murine model of globoid cell leukodystrophy. J. Neuropathol. Exp. Neurol. *58*, 644–653.

67. Tohyama, J., Matsuda, J., and Suzuki, K. (2001). Psychosine is as potent an inducer of cell death as C6-ceramide in cultured fibroblasts and in MOCH-1 cells. Neurochem. Res. *26*, 667–671.

68. Jatana, M., Giri, S., and Singh, A.K. (2002). Apoptotic positive cells in Krabbe brain and induction of apoptosis in rat C6 glial cells by psychosine. Neurosci. Lett. *330*, 183–187.

69. Zaka, M., and Wenger, D.A. (2004). Psychosine-induced apoptosis in a mouse oligodendrocyte progenitor cell line is mediated by caspase activation. Neurosci. Lett. *358*, 205–209.

70. Hu, F., Ku, M.C., Markovic, D., Dzaye, O., Lehnardt, S., Synowitz, M., Wolf, S.A., and Kettenmann, H. (2014). Glioma-associated microglial MMP9 expression is upregulated by TLR2 signaling and sensitive to minocycline. Int. J. Cancer *135*, 2569–2578.

71. Li, Z., Zeng, Y., Chen, X., Li, Q., Wu, W., Xue, L., Xu, H., and Yin, Z.Q. (2016). Neural stem cells transplanted to the subretinal space of rd1 mice delay retinal degeneration by suppressing microglia activation. Cytotherapy *18*, 771–784.

72. Fei, M., Wang, H., Zhou, M., Deng, C., Zhang, L., and Han, Y. (2020). Podoplanin influences the inflammatory phenotypes and mobility of microglia in traumatic brain injury. Biochem. Biophys. Res. Commun. *523*, 361–367.

73. Bradbury, A.M., Bagel, J.H., Nguyen, D., Lykken, E.A., Pesayco Salvador, J., Jiang, X., Swain, G.P., Assenmacher, C.A., Hendricks, I.J., Miyadera, K., et al. (2020). Krabbe disease successfully treated via monotherapy of intrathecal gene therapy. J. Clin. Invest. *130*, 4906–4920.

74. Li, Y., Miller, C.A., Shea, L.K., Jiang, X., Guzman, M.A., Chandler, R.J., Ramakrishnan, S.M., Smith, S.N., Venditti, C.P., Vogler, C.A., et al. (2021). Enhanced Efficacy and Increased Long-Term Toxicity of CNS-Directed, AAV-Based Combination Therapy for Krabbe disease. Mol. Ther. Published online December 31, 2020. https://doi.org/10.1016/j.ymthe.2020.12.031.

75. Sakai, N., Inui, K., Tatsumi, N., Fukushima, H., Nishigaki, T., Taniike, M., Nishimoto, J., Tsukamoto, H., Yanagihara, I., Ozono, K., and Okada, S. (1996). Molecular cloning and expression of cDNA for murine galactocerebrosidase and mutation analysis of the twitcher mouse, a model of Krabbe's disease. J. Neurochem. *66*, 1118–1124.

76. Gray, S.J., Foti, S.B., Schwartz, J.W., Bachaboina, L., Taylor-Blake, B., Coleman, J., Ehlers, M.D., Zylka, M.J., McCown, T.J., and Samulski, R.J. (2011). Optimizing promoters for recombinant adeno-associated virus-mediated gene expression in the peripheral and central nervous system using self-complementary vectors. Hum. Gene Ther. *22*, 1143–1153.

77. Grieger, J.C., Soltys, S.M., and Samulski, R.J. (2016). Production of Recombinant Adeno-associated Virus Vectors Using Suspension HEK293 Cells and Continuous Harvest of Vector From the Culture Media for GMP FIX and FLT1 Clinical Vector. Mol. Ther. *24*, 287–297.

78. Dolcetta, D., Perani, L., Givogri, M.I., Galbiati, F., Amadio, S., Del Carro, U., Finocchiaro, G., Fanzani, A., Marchesini, S., Naldini, L., et al. (2006). Design and optimization of lentiviral vectors for transfer of GALC expression in Twitcher brain. J. Gene Med. *8*, 962–971.

79. Domowicz, M.S., Sanders, T.A., Ragsdale, C.W., and Schwartz, N.B. (2008). Aggrecan is expressed by embryonic brain glia and regulates astrocyte development. Dev. Biol. *315*, 114–124.

80. Smith, B.R., Santos, M.B., Marshall, M.S., Cantuti-Castelvetri, L., Lopez-Rosas, A., Li, G., van Breemen, R., Claycomb, K.I., Gallea, J.I., Celej, M.S., et al. (2014). Neuronal inclusions of α-synuclein contribute to the pathogenesis of Krabbe disease. J. Pathol. *232*, 509–521.